

# Aerodynamic Control of Coupled Body-Wake Interactions

Thomas J. Lambert<sup>\*</sup>, Bojan Vukasinovic<sup>†</sup> and Ari Glezer<sup>‡</sup>

*Woodruff School of Mechanical Engineering,  
Georgia Institute of Technology, Atlanta, GA 30332-0405*

The unsteady interactions between fluidic actuators and the cross flow over the aft end of a moving bluff body are exploited for modification of the global unsteady aerodynamic loads in wind tunnel experiments using a moving axisymmetric model. The model moves in combined pitch and yaw which is designed to mimic the natural unstable motion of a similar airborne platform in the absence of roll. Actuation is effected using an azimuthally-segmented array of four aft-facing synthetic jet modules around the tail end of a model, and motion is effected by eight mounting wires that are attached to servo motors for time-dependent, six degrees of freedom motion along a prescribed trajectory. Enhancement and suppression of stabilizing aerodynamic loads on the model are each investigated using coupled force and moment measurements and stereo particle image velocimetry in the near wake, at reduced frequencies of up to 0.26. The present measurements show significant suppression (up to 80%) and augmentation (up to 40%) of the platform's motion-induced aerodynamic forces or moments with concomitant controlled deflection and decoupling of the near-wake from the motion of the body. The present investigations show that the effects of actuation on the near wake of the body are comparable to the effects of its baseline unstable pitch and yaw motion and therefore can be used to induce aerodynamic loads that cancel or enhance the baseline loads to effect dynamic steering and stabilization.

## Nomenclature

$a_n$	weighted time dependence of $n$ th POD mode	$St_D$	Strouhal number
$A_J$	actuator orifice cross-sectional area	$t$	time relative to start of motion or actuation
$C_{D,S,L}$	coefficient of drag, side, and lift forces	$t_{ref}$	reference time for 3-D velocity surfaces
$C_{R,M,Y}$	coefficient of roll, pitch, and yaw moments	$u,v,w$	velocity components in $x$ , $y$ , and $z$ directions
$C_\mu$	jet momentum coefficient	$U_J$	maximum jet expulsion velocity
$D$	axisymmetric body diameter	$U_0$	free stream velocity
$E_n$	energy contribution of $n$ th POD mode	$\vec{V}$	measured 3-D velocity vectors
$f$	body motion frequency	$x,y,z$	reference coordinate system
$f_{act}$	synthetic jet frequency	$\vec{X}$	state vector used for POD analysis
$F_{D,S,L}$	aerodynamic drag, side, and lift force	$y_c, z_c$	measured translation of wake velocity deficit
$h_s$	body backward-facing step height	$\alpha_{x,y,z}$	angles reference to $x$ , $y$ , $z$ (roll, pitch, yaw)
$k$	model reduced frequency	$\Delta$	$y$ and $z$ grid spacing in SPIV measurements
$L$	body chord length	$\vec{\varphi}_n$	$n$ th velocity vector POD modes
$M_{R,P,Y}$	aerodynamic roll, pitch, and yaw moments	$\vec{\varphi}_{n,\zeta}$	derived $\zeta$ from velocity POD modes
$n$	POD mode number	$\lambda_n$	eigenvalue of the corresponding POD mode $\vec{\varphi}_n$
$N$	max number of independent POD modes	$\rho$	air density
$R$	axisymmetric body radius	$\theta_y, \theta_z$	angular deflections of wake velocity deficit
$R_c$	Coanda surface radius	$\tau$	body pitching period
$Re_D$	Reynolds number	$\zeta$	streamwise vorticity

<sup>\*</sup> Graduate Research Assistant, AIAA Member.

<sup>†</sup> Research Engineer, AIAA Member.

<sup>‡</sup> Professor, Associate Fellow AIAA.

## I. Technical Background

The present work focuses on manipulation of the global unsteady aerodynamic loads on a dynamic axisymmetric bluff body by active modification of the coupling between the flow over the body and its near wake. This coupling is altered using active flow control that effects a time-dependent partial flow attachment of a nominally axisymmetric separating shear layer over the aft end of the body and thereby imposes asymmetric distortion of the near wake that has a profound effect on its evolution and stability (e.g., Wu et al.<sup>1</sup>). For this control strategy, attachment is effected using fluidic actuation frequencies that are sufficiently high above the receptivity bandwidth of the natural unstable modes of the near wake (e.g., Erk<sup>2</sup>, Smith et al.<sup>3</sup>, Amitay et al.<sup>4</sup>, Honohan et al.<sup>5</sup>, Glezer et al.<sup>6</sup>).

Active control of flow separation and thereby of global aerodynamic performance can be significantly enhanced by hybrid (active and passive) control that exploits the interaction of the actuation jets with adjacent solid surfaces, or the Coanda effect, which has been investigated extensively since the 1940s (e.g., Newman<sup>7</sup>). This effect has also been the basis of circulation control over lifting surfaces in numerous aerodynamic systems (e.g., Englar<sup>8</sup>). Hybrid flow control was also demonstrated by Nagib et al.<sup>9</sup> who combined a short backward-facing step with a jet to control local separation. This approach was later used for controlling internal flows, for example, by Lo et al.<sup>10</sup>, who controlled separation in adverse pressure gradients in a diffuser.

Since the Coanda effect is associated with the attachment of an inherently separated flow to a solid surface, this flow configuration presents a unique opportunity to create asymmetric pressure distributions and net aerodynamic forces on various bluff bodies through differential, asymmetric activation. Freund and Mungal<sup>11</sup> reduced the aerodynamic drag of axisymmetric bodies by up to 30% using induced attachment at the aft corner of the body by steady, circumferentially-uniform blowing over Coanda surfaces. Rinehart et al.<sup>12,13</sup> demonstrated generation of a asymmetric force on an aerodynamic platform using the interaction of a single synthetic jet with an integrated axisymmetric azimuthally-segmented Coanda tail surface along a backward facing step. In a related investigation, McMichael et al.<sup>14</sup> exploited this flow control approach to the separated base flow of an axisymmetric 40 mm spin-stabilized projectile to effect aerodynamic steering forces and moments that were sufficient to control the trajectory of the projectile in flight. Corke et al.<sup>15</sup> reported alteration of the drag and side forces on an axisymmetric body using tangential plasma actuation placed upstream of a Coanda surface. Abramson et al.<sup>16,17</sup> extended the Coanda actuation methodology to effect prescribed (asymmetric) side forces by using four individually controlled azimuthally distributed synthetic jets within the rearward-facing step of the tail and demonstrated that the induced forces can be used to effect steering during flight and trajectory stabilization. Finally, Lambert et al.<sup>18</sup> showed that the trajectory of a free-moving axisymmetric model in one degree of freedom can be significantly suppressed or enhanced with appropriate timing and modulation of the actuation, and this could lead to significant directional control authority for free flight aerodynamic bodies.

Control of the aerodynamic forces on axisymmetric platforms builds on numerous earlier investigations of the uncontrolled base flow and its natural instabilities. The basic motions of spinning projectiles, including natural nutation and precession linear and nonlinear instabilities, induced by Magnus, damping, and normal forces and moments are discussed in detail in the classical work of Nicolaides<sup>19</sup>. The instabilities of symmetric projectiles in the presence and absence of spin were discussed in detail by Murphy<sup>20</sup>. While spin-stabilized projectiles are gyroscopically stable to axisymmetric moment instability, they are susceptible to roll resonance<sup>21</sup>, and spin-yaw lock in<sup>22</sup>, which add complicated non-linear effects to the projectile dynamics that are in general hard to correct for. In recent years considerable attention has been devoted to the development active control approaches for both fin- and spin-stabilized projectiles, including aerodynamic forces induced by a piezoelectric-articulated nose section<sup>23</sup>, synthetic jet actuation on a spinning projectile<sup>24</sup>, and the swerve response of finned and spin-stabilized projectiles to generic control forces<sup>25,26</sup>.

An inherent difficulty with wind tunnel investigations of nominally ‘free’ aerodynamic bodies is related to their mounting in the tunnel’s test section. Ideally, the model support should cause little or no aerodynamic interference (such as magnetic-force support<sup>27</sup>), but most conventional support systems have relied on some form of side or rear sting mounts that can interfere with the flow around the body and especially in its wake. An alternative support, aimed at minimizing flow interference, was utilized by Abramson et al.<sup>16,17</sup> and later on by Lambert et al.<sup>28</sup>, who supported their model using thin wires. In the present investigations, an axisymmetric bluff body integrated with individually-controlled miniature fluidic actuators is wire-mounted on a programmable 6-DOF (x/y/z-translation & pitch/yaw/roll) eight-wire traverse that is electromechanically driven by a dedicated feedback controller to remove the parasitic mass and inertia of the dynamic support system and of the model. The interactions between the

actuation and the cross flow are investigated using stereo PIV, a motion analysis system, and time-resolved aerodynamic forces and moments.

The present investigations build on the earlier work of Lambert et al.<sup>29,30</sup> who demonstrated that the aerodynamic loads induced by an azimuthal array of hybrid synthetic jet actuators on an axisymmetric bluff body are comparable to the corresponding aerodynamic loads that are generated during pitch motion over a broad range of frequencies in the absence of actuation, and in addition, the vortex shedding could be excited in this pitching direction. The goal of the current investigation is to demonstrate that this control approach is robust enough to control the wake in *combined pitch and yaw*. Therefore, as the realistic body undergoes unstable, combined pitch and yaw motion the actuation has the control authority necessary for trajectory stabilization without spin.

## II. Experiment and Control Methodologies

The current investigation studies flow around a bluff body wind tunnel model ( $D = 90$  mm,  $L = 165$  mm) which is shown in Figures 1a and b (side and back, views). The model is scaled based on the earlier investigations of McMichael et al.<sup>14</sup> and Abramson et al.<sup>16,17</sup>, and is the same model used in Lambert et al.<sup>18,29,30</sup>. The model is built using both stereo-lithographed and aluminum components. This model is driven in motion using eight support wires which are fixed into the center aluminum piece, and the rest of the model (containing synthetic jet actuators in the aft end) is fastened together to the central aluminum spine. Aerodynamic control loads are generated using an azimuthal array of four aft facing independently-driven synthetic jet actuators (each with a rearward facing area  $A_J = 0.38$  mm  $\times$  34.3 mm) that are each equally distributed around the perimeter of the tail section in an adjoining backward-facing step with height of  $h_s = 1.5$  mm. The downstream end of the model has a Coanda surface ( $R_c = 12.7$  mm), with grooves along the jet orifice edges that guide the engendered jet flow. Actuation leads to the partial attachment of the flow along the inner grooves of the Coanda surface resulting in a reaction force by turning of the cross flow into the near wake. In the present investigations, the maximum jet expulsion velocity of each jet is set to  $U_J = 40$  m/s (a momentum coefficient of  $C_\mu = \frac{4U_J^2 A_J^2}{U_0^2 \pi D^2} = 4 \cdot 10^3$ ), at an actuation frequency of  $f_{act} = 1.1$  kHz.

The axisymmetric model is wire mounted in an open-return wind tunnel at Georgia Tech (0.91 m  $\times$  0.91 m tests section, with a free stream velocity of  $U_0 = 30$  m/s, yielding  $Re_D = 1.8 \cdot 10^5$ ) using an eight servo-motor traverse capable of motion in six degrees of freedom over a broad range of frequencies (Figure 2a). The eight support steel wires (0.96 mm diameter) are selected to be thin enough to decouple their vortex shedding from the model, while thick enough to minimize translational and rotational vibrations. Each support wire is fastened to a servo motor, with an in-line load cell, and in addition, each motor is attached to an external spring for pretension. The flow control approach utilizes embedded synthetic jets in the axisymmetric model, where the connection for the actuators is enabled by means of electrical wires weaved along the back four support wires and through the tunnel walls, while the support wires provide electrical ground. The traverse is designed (based on earlier 1-DOF investigations

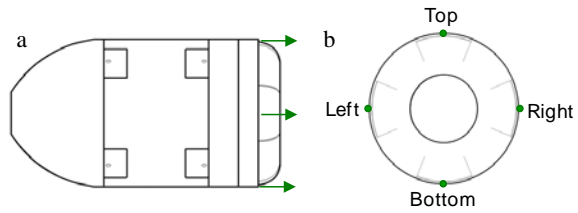


**Figure 1.** Side (a) and upstream (b) views of the centered wind tunnel model with four hybrid fluidic actuators marked in green.

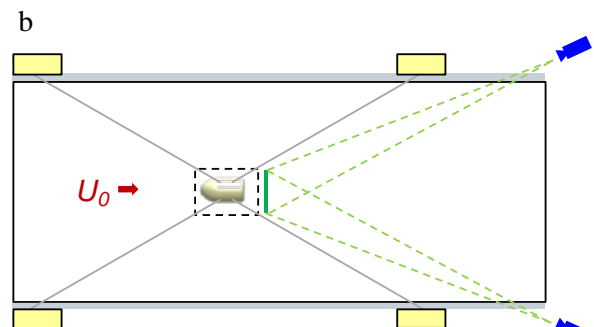


**Figure 2.** Six degree of freedom traversing mechanism utilizing eight support wires, each connected to an in-line load cell, a servo-actuator, and a pre-tensioned spring (a), and a top view schematic of the SPIV interrogation region and camera orientation (b).

by Lambert et al<sup>18</sup>) to provide 3-D translations up to 40 mm and angular motions in pitch, yaw and roll of up to 12°, 9°, and 6°, respectively, at 1 Hz, with smaller amplitude motions up to 50 Hz. The forces and moments on the system (model and wires) are calculated from the measured load cell tensions projected onto the model, and the resulting aerodynamic forces and moments are computed relative to the wind-off conditions (the form drag load on each wire is also estimated and subtracted). An external six-camera, high-speed motion analysis Vicon tracking system measures the model's motion in six degrees of freedom (6-DOF) and is also used for feedback for the model trajectory controller. The model is moved in harmonic motion in combined pitch ( $\alpha_z$ ) and yaw ( $\alpha_z$ ), 90° out of phase, with an amplitude of 3° at frequencies from 1Hz to 15Hz ( $0.017 < k = \pi f L / U_0 < 0.259$ ), which is referred to as 1:1 Lissajous rotation. In addition to the aerodynamic forces and moments, the velocity in the wake is measured using a Stereo Particle Image Velocimetry (SPIV) system as shown, with a top view, in Figure 2b. There are two triggered 14-bit cameras, each at an angle of 25 degrees (shown in blue) which resolve all three components of the velocity field in an interrogation region of  $1.3D \times 1.3D$  at a fixed streamwise location of  $1D$  downstream of the aft end of the model (1.9D downstream of the axis of pitch/yaw rotation).

The model motion is controlled through a trajectory tracking controller which was utilized in two previous studies by Lambert et al.<sup>29,30</sup> and is shown in Figure 3. The two command inputs are a time trace for the desired model trajectory in 6-DOF, and a time trace for the actuation commands to modulate all four synthetic jet resonance waveforms (each at an inner frequency of  $f_{act}$ ) for the desired induced jet effects. The commanded motion is converted into eight motor commands in an “inner loop controller” involving using the motor encoders and load cells as the sensors of a PID controller for disturbance rejection. In addition, an external motion analysis system is implemented to measure the real-time position of the model in 6-DOF. This position measurement is used in an “outer loop controller” to adjust the command of the inner loop to allow for accurate trajectory tracking with disturbance rejection. The outer loop uses a PID feedback controller that is set such that the commanded and actual trajectories converge within ten seconds of the motion onset. The real time load cell tensions are used to extract the aerodynamic forces and moments on the model by measuring the net force on the model and subtracting the inertia, gravitational effects, and drag of the mounting wires predicted by the model’s measured trajectory.

### III. Static Model: The Near-Wake Structure

The near wake behind the stationary model at  $Re_D = 1.8 \cdot 10^5$  is measured in the interrogation region previously discussed in Section II in Figure 2b. The result is a 3-D velocity flow field with the streamwise velocity,  $u$ , in the  $x$  direction, and the cross stream velocities,  $v$  and  $w$ , in the  $y$  and  $z$  directions, respectively. The interrogation region is chosen to be at a fixed streamwise location of  $1D$  downstream of the aft end of the model, spanning  $1.3D$  in  $y$  and  $1.3D$  in  $z$ , ( $y = \pm 1.3R$ , and  $z = \pm 1.3R$ , centered about the model). The resulting stream surface of the flow is shown in Figure 4, with a  $64 \times 64$  grid of time averaged velocity vectors,  $\bar{V}$ , over 600 instantaneous measurements. This surface is calculated by taking the location at which each  $\bar{V}$  was measured and adding on a distance of  $\bar{V} \cdot t_{ref}$ , where  $t_{ref} = 2$  ms. This surface is also colored by the streamwise velocity

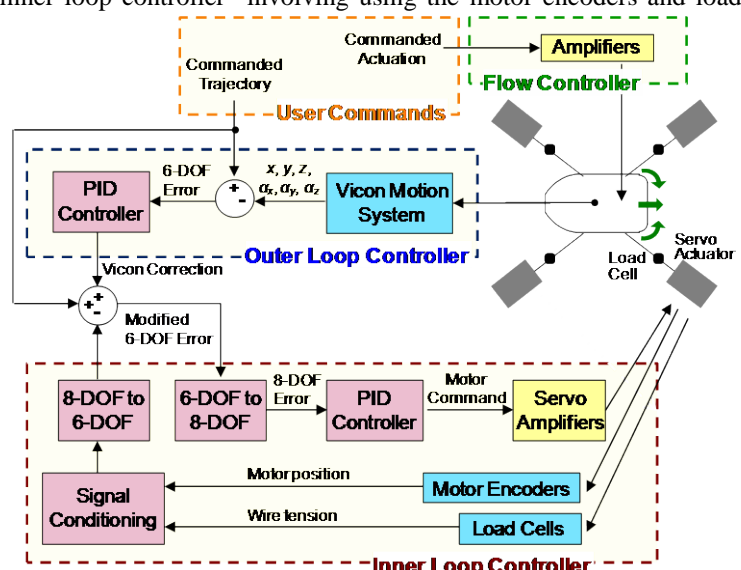


Figure 3. Schematics of the traverse trajectory tracking controller.

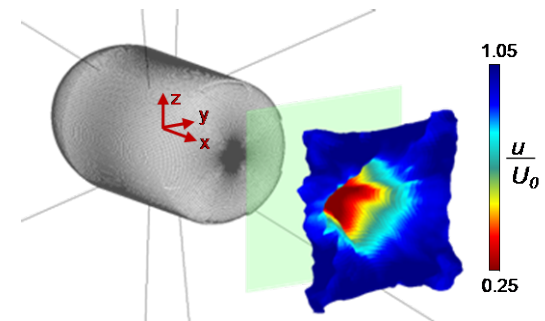


Figure 4. SPIV on a stationary model with  $Re_D = 1.8 \cdot 10^5$  shown to scale with the global coordinate system in red, the interrogation region in green, and a stream-surface created by  $\bar{V} \cdot t_{ref}$  and contoured by  $|\bar{V}|$ , where  $\bar{V}$  is the measured 3-D velocity field and  $t_{ref} = 2$  ms.

component, which is the dominant component of the velocity field, and ranges from  $0.3U_0$  in the center of the wake deficit behind the model to nominally  $U_0$  in the free stream, with slight reduction in the wake of the wires. For reference, the model with wires is shown in gray, the interrogation region is shown in green, and the global coordinate system ( $x,y,z$ ) is shown in red.

An in depth analysis of the wake velocity flow field for the stationary model is shown in Figure 5. The equivalent streamwise velocity component,  $u$ , to Figure 4 is shown in Figure 5a, in a planar interrogation region, and in addition the projections of the wires are shown in gray. It is noted that the baseline flow is not completely axisymmetric due to the geometry of aft end of the model, where the backward-facing steps that house the inactive actuators (see Figure 1b) locally displace flow from the Coanda surface, which leads to an extension of the wake deficit region in the vertical and horizontal directions. The commensurate cross-stream velocity components ( $v$  and  $w$ ) are shown in Figure 5b as a quiver plot alongside with a contour of the streamwise vorticity,  $\zeta$ , calculated from these velocity components. It is noted that the cross-stream velocity magnitude is significantly smaller than the streamwise velocity, with a maximum values of  $\sim 0.2U_0$  at the location of the shear layer, and approaching values of 0 in both of the center of the window and in the free stream. Although this flow is nominally converging to center, there is a faint vortex structure that is present, which is again contributed to the geometry of the aft end of the model: the vortex structure is essentially a weak 8-lobe structure due to slowing of the radial velocity downstream of the inactive actuators. It is also noted that there are slight contributions to the streamwise vorticity due to the wires in the corners of the interrogation region. To further investigate the structure of the wake, instantaneous velocity vectors that are used to calculate the average fields in Figures 5a and b are also used to extract the Proper Orthogonal Decomposition (POD) modes of the wake:

$$\vec{X}(t) - \langle \vec{X} \rangle = \sum_{n=1}^N a_n(t) \cdot \vec{\varphi}_n \quad (\text{Eq. 1})$$

where  $\vec{X}(t)$  is an instantaneous state vector in a dataset to be reconstructed with POD modes,  $\langle \vec{X} \rangle$  is the time averaged value of  $\vec{X}(t)$ ,  $\vec{\varphi}_n$  is the  $n$ th POD mode,  $a_n(t)$  is the weighted time dependence of the  $n$ th POD mode, and  $N$  is the rank of the data set (i.e. the maximum independent vectors either spatially or in time). The analysis in this paper for all presented POD modes is performed extracting the first 30 modes when the state  $\vec{X}(t)$  is chosen to be a column vector of  $u(t)$ ,  $v(t)$ , and  $w(t)$  at a given time concatenated vertically, and the dataset includes 600 time realizations. This POD analysis is first performed on the baseline flow in Figures 5a and b and the energy contribution of the first 30 modes is shown in Figure 5c. The energy of each mode is defined as:

$$E_n(\%) = \frac{100|\lambda_n|^2}{\sum_{i=1}^N |\lambda_i|^2} \quad (\text{Eq. 2})$$

Where  $\lambda_n$  is the eigenvalue of the corresponding eigenmode  $\vec{\varphi}_n$ . Based on the energy distribution, it appears the first two modes are more prominent than the rest, having a higher than 4% energy contribution, while energy fractions become reduced to less than 1% by the ninth mode.

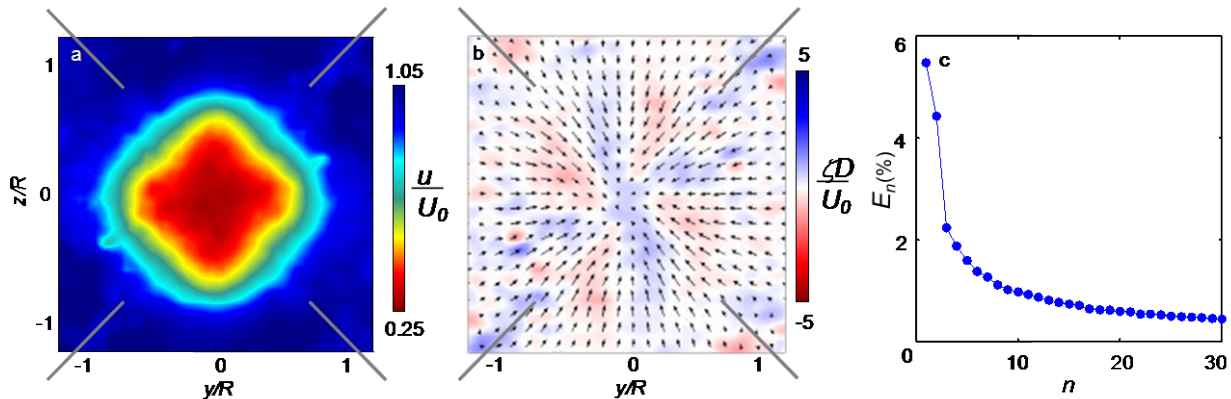


**Figure 5.** Contour plots of the base flow streamwise velocity (a) and streamwise vorticity (b), and POD mode energy contributions for the first 30 modes of the combined velocity components ( $u,v,w$ ) (c) for  $Re_D = 1.8 \cdot 10^5$  with the cross-stream location of the mounting wires shown in gray.

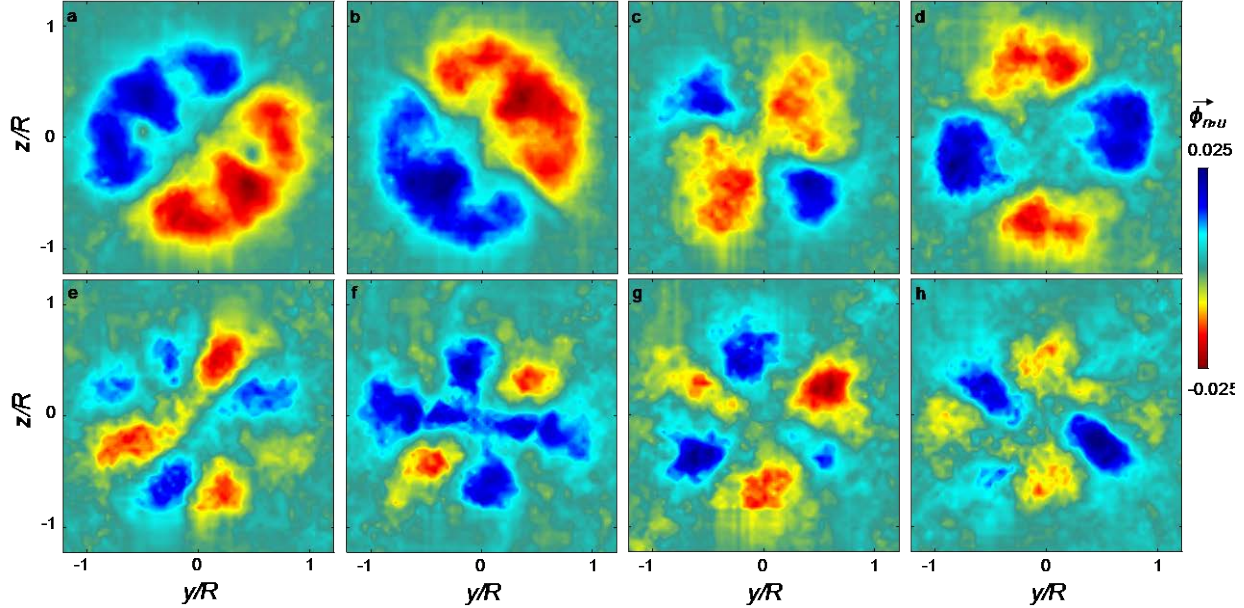


**Figure 6.** Contour plots of the streamwise velocity component of the POD modes,  $\vec{\varphi}_{n,u}$ , with mode number,  $n = 1$  (a), 2 (b), 3 (c), 4 (d), 5 (e), 6 (f), 7 (g), and 8 (h) for the base flow at  $Re_D = 1.8 \cdot 10^5$ .

The POD modes of the subset of  $\vec{\varphi}_n$  that correspond to the streamwise velocity,  $\vec{\varphi}_{n,u}$  are shown in Figure 6 with  $n = 1$  (Figure 6a), 2 (Figure 6b), 3 (Figure 6c), 4 (Figure 6d), 5 (Figure 6e), 6 (Figure 6f), 7 (Figure 6g), and 8 (Figure 6h). The first two modes shown in Figures 6a and b are a rotated pair that represent a two-fold symmetry of vortex shedding from the model top left to or from the bottom right (Figure 6a), and the bottom left to or from the top right (Figure 6b). It is important to note that this wake structure is not related to the mounting wires, which make a  $53^\circ$  angle from the top in this frame of view, and instead seem to line up with  $45^\circ$ , which is the azimuthal center between two of the jet actuators. This suggests that the primary shedding of the model (and therefore the primary change in the wake deficit) is biased away from the backward facing steps when the jets are inactive and the model is stationary (see Figure 1b and compare to the shape of Figures 6a and b). Another interesting feature about this dataset is the effects of the wire are not as prominent as they were in Figure 5, which suggests that the effect of the wire is mostly invariant with time (relative to the wake time scales) and gets subtracted off when the mean is subtracted for POD analysis. The second and third modes (Figures 6c and d) again form a rotated pair which now has a four-fold symmetry instead of a two-fold symmetry and this pattern continues into Figure 6e which has an apparent 8 fold symmetry. The pairing of POD modes stops at the fifth mode, where the sixth mode in Figure 6f significantly differs from the fifth mode in Figure 6e, where it is no longer a rotated version of the previous mode, and it is also the first mode to have a predominant sign (i.e., the velocity change in the center is much greater than the two regions of opposite sense around it). The seventh mode in Figure 6g is the first mode that shows a six fold symmetry in the velocity fluctuations. The final eighth mode in Figure 6h also shows 6 regions of alternating sign, but is dominated mostly by two neighboring regions of the same sense in the bottom right and top left.

The remaining subset of  $\vec{\varphi}_n$  that was used to present the streamwise velocity modes in Figure 6 are used to extract the modes in the cross-stream velocities  $\vec{\varphi}_{n,v}$  and  $\vec{\varphi}_{n,w}$ . These two velocity modes are then used to calculate their respective streamwise vorticity:

$$\vec{\varphi}_{n,\zeta} = \frac{d\vec{\varphi}_{n,w}}{dy} - \frac{d\vec{\varphi}_{n,v}}{dz} \quad (\text{Eq. 3})$$

It is emphasized that this vorticity mode is derived from the result of the POD analysis and is not a direct result of the POD analysis (i.e., it is not a POD mode of the vorticity field). The derivatives are taken in Eq. 3 using a 3x3 stencil and a first order centered analysis, and therefore  $\vec{\varphi}_{n,\zeta}$  is normalized by the grid spacing between velocity vectors,  $\Delta = 1.7\text{mm}$ , which is uniform in the  $y$  and  $z$  directions. The resultant normalized cross-stream velocity modes and their derivative normalized vorticity are plotted in Figure 7 with the first eight modes, similar to Figure 6. The same pairing of the first and second mode seen in the streamwise velocity in Figures 6a and b is observed in the cross-stream velocities in Figures 7a and b, each with a predominant counter-rotating vortex pair in the top left

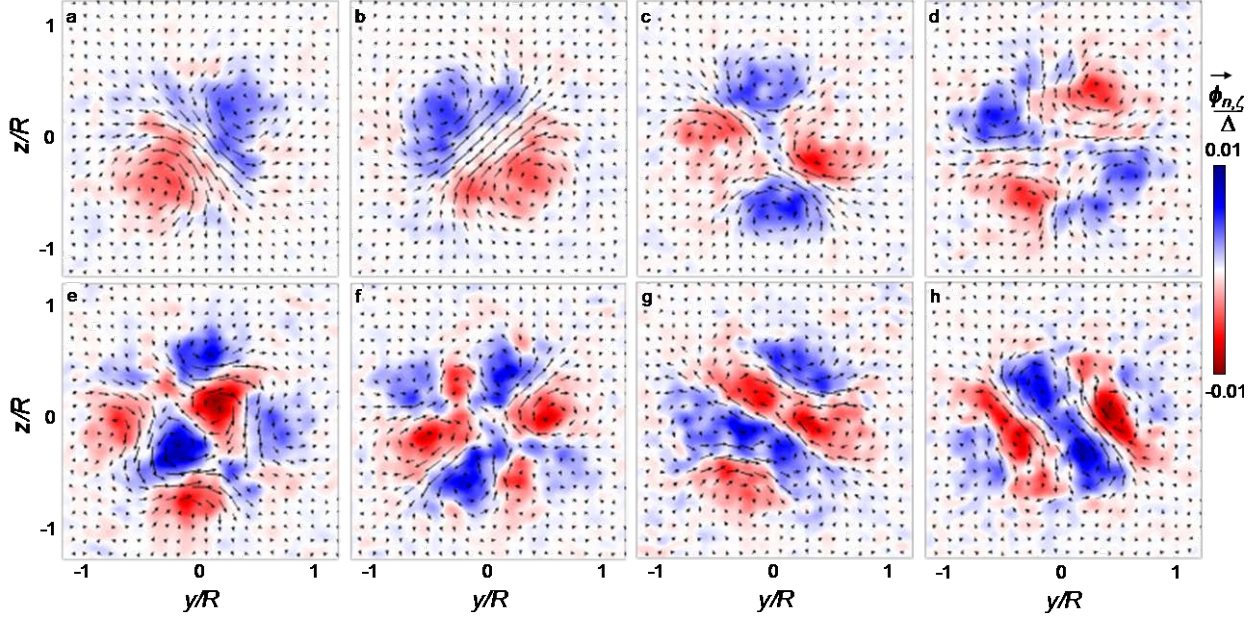


**Figure 7.** Quiver plots of the cross-stream velocity components of the POD modes,  $\bar{\phi}_{n,v}$  and  $\bar{\phi}_{n,w}$ , with mode number  $n = 1$  (a), 2 (b), 3 (c), 4 (d), 5 (e), 6 (f), 7 (g), and 8 (h), colored by their streamwise vorticity,  $\bar{\phi}_{n,\zeta}$ , for the base flow at  $Re_D = 1.8 \cdot 10^5$ .

to/from bottom right and top right to/from bottom left, respectively. It is also noted that the order of these pair modes could change depending on the instantaneous images (i.e., due to the left-right symmetry of this model there is no reason to believe one side should always have dominant energy). The next mode pair in the third and fourth mode in Figures 7c and d now shows two counter-rotating streamwise vortex pairs in agreement with Figure 6c and d. Another interesting feature that appears in the streamwise vorticity of these modes is that the maximum value occurs at locations where the sign of the streamwise velocity mode changes (compare Figures 7a-d to Figures 6a-d). The fifth and sixth modes in Figures 7e and f, respectively, introduce more vortex structures with some regions not clearly defined, and the seventh and eighth modes in Figures 7g and h, respectively, introduce a new feature of a streamwise vortex that crosses the centerline of the model which was not seen in lower modes. The last four modes also appear to have a paired structure in the cross-stream velocity modes, while Figures 7e and f appear similar in structure to each other, as do Figures 7g and h. However, these same cases show deviations in their respectively streamwise velocity modes in Figures 6e and f and Figures 6g and h, respectively, showing that different modes could have a similar structure in one velocity component and not other components. It is shown in Figure 6 and 7 that as the mode number  $n$  increases, the structure of the POD mode starts to lose organization, and therefore for all of the following POD datasets shown in this paper, only the first four modes are analyzed for brevity.

#### IV. Motion- and Actuation- Induced Aerodynamic Loads

The remainder of this investigation focuses on three scenarios: a dynamic bluff body, a stationary bluff body with fluidic actuation, and a dynamic bluff body with fluidic actuation. The induced dynamics are chosen to be 1:1 Lissajous rotation (combined pitch,  $\alpha_y$ , and yaw,  $\alpha_z$ ), where pitch lags the yaw by  $90^\circ$  phase, and both have an amplitude of  $3^\circ$ , as this type of motion corresponds to the expected natural unstable motion of an equivalent airborne body, in the absence of roll. The frequency of this motion is varied during this study, and a representative quasi-steady frequency of  $k = 0.017$  is investigated first and shown in Figure 8. This executed motion is shown in Figure 8a, with pitch in cyan and yaw in blue. The corresponding induced lift and side force coefficients ( $C_L$  and  $C_S$ , respectively) on the model are shown in Figure 8b, as an average of 50 instantaneous measurements, and the force coefficients are derived from the measured forces by  $C = 8F/(\rho\pi U^2 D^2)$ . There is a presence of two higher frequencies in both  $C_L$  and  $C_S$ , one that corresponds to the wake shedding frequency of 83Hz ( $k = 1.434$ , that corresponds to  $St_D = fD/U_0 = 0.234$ , and previously measured in Lambert et al.<sup>30</sup>), and another that corresponds to a lower frequency at  $\sim 12$  Hz ( $k = 0.207$ ), which is attributed to the instability frequency of the 1:1 Lissajous motion on this model without spin. The two force coefficients are plotted against each other in Figure 8c, where they trace out a circle with radius of 0.11, in addition to the presence of the two instabilities. The representative fluidic actuation is

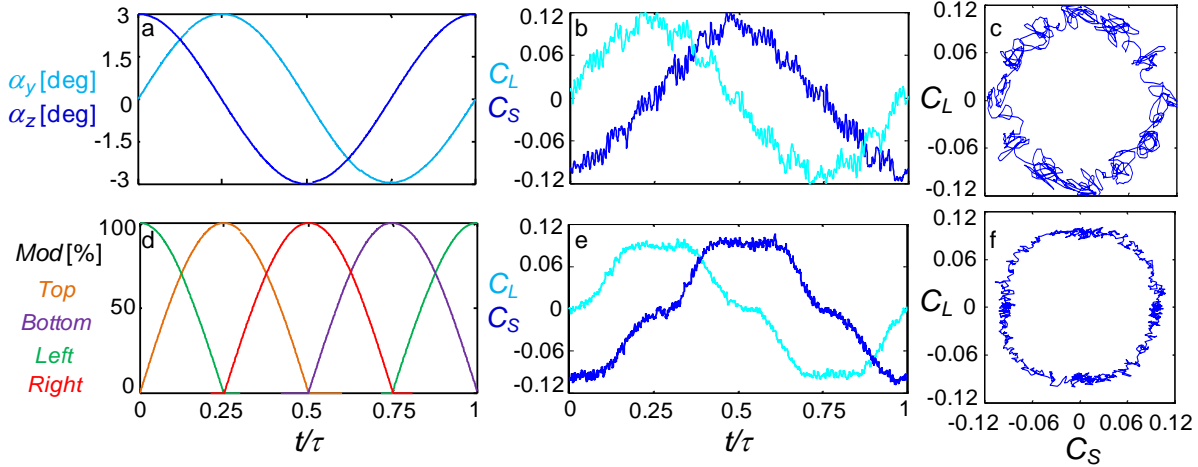


**Figure 8.** Side and lift forces (b,c) induced on a model undergoing 1:1 Lissajous rotation with a phase difference of 90° (a), and the corresponding forces (e,f) on a stationary model by the actuation algorithm (d) for  $k = 0.017$ .

chosen to induce forces on a *stationary* model, mimicking the forces that are equal to the flow-induced forces on a *moving* model. To achieve this, the synthetic jet actuation waveform, which has a frequency of  $f_{act} = 1.1\text{kHz}$ , is generated by an external function generator which delivers a maximum  $C_\mu = 0.004$  at a full modulation command. Independent modulations are created and sent to all four jets by the controller in Figure 3, which allows control of  $C_\mu$  in the range of 0 to 0.004. This same methodology was used before in Lambert et al.<sup>18</sup> and Abramson et al.<sup>17</sup> for the same model. Based on this prior work, the desired modulation waveform is chosen to be an overlapping sinusoidal modulation to all four jets, and is shown in Figure 8d. The corresponding  $C_L$  and  $C_S$  that are induced by this actuation are shown in Figure 8e, which indicates good agreement in magnitude with the motion-induced  $C_L$  and  $C_S$  in Figure 8b, with the exception that the lower frequency instability attributed to the spinning motion is no longer detected, even though the shedding frequency is still present. These two induced force coefficients are plotted against each other in Figure 8f, which shows a less circular trace than in Figure 8c, which is due to the actuation effect in Figure 8e being induced slightly faster than the effect of the motion in Figure 8b. Nevertheless, the fact that the magnitude of the actuation-induced forces are of the same order as the motion-induced forces in Figure 8 suggests that active fluidic control has sufficient authority to significantly control the motion-induced forces for the preselected 1:1 Lissajous rotation.

Next, the frequency of the two patterns shown in Figure 8 is varied, while keeping the motion amplitude and fluidic modulation amplitude fixed. The resulting variations in the  $C_L$  and  $C_S$  trace shown in Figures 8c and f throughout higher frequencies is shown in Figure 9, with the resulting fluidic induced forces in green, and the motion-induced forces in blue. Figure 9a shows  $k = 0.017$ , which corresponds to the cases in Figure 8c and f plotted with each other. As  $k$  is increased to 0.086 (Figure 9b), the motion-induced forces start to increase while the actuation-induced forces remain roughly invariant. It is noted that all of the plots in Figure 9 are plotted in a 1 second time trace that is the result of 50 averages to visualize the variation of the force coefficients on the same time scale. Near the motion-resonance that was detected in Figure 8b of  $k = 0.207$ , there is around a 125% growth in both the motion induced  $C_L$  and  $C_S$  shown in blue in Figures 9c and d (with  $k = 0.172$  and 0.207), respectively. However, the actuation-induced force coefficient's magnitude shown in green in Figure 9c and still remains roughly invariant, with slight changes in its shape to have prominent maxima at the location in the paths where either  $C_S = 0$  or  $C_L = 0$ . When the frequency is increased past the motion-resonance frequency to  $k = 0.259$  (Figure 9e), the motion-induced lift force begins to decrease in magnitude to values similar to its lower frequencies (compare the blue line in Figure 9e with Figures 9a and b). The lack of frequency variation in the actuation-induced forces continues at  $k = 0.259$ , shown in Figure 9e in green (compare Figure 9e and Figure 9d). The absence of the frequency variation of the actuation induced force coefficients in the range of  $k = 0.017$  to 0.259 is commensurate with the lack of a spectral frequency in Figure 8e, where the motion-induced response has a natural frequency present within the range of the frequency variation in Figures 9a-e (see Figure 8b). To test this hypothesis, the actuation-induced forces are driven at the higher resonance frequency of  $k = 1.434$  (83 Hz), shown in Figure 9f in green. This frequency is out of the range of the current wire-traverse control authority and therefore the motion-induced forces for this frequency are omitted from Figure 9f. Two features become prominent at this resonance frequency: the response becomes biased in the side force coefficient, and the variation of the recorded actuation-

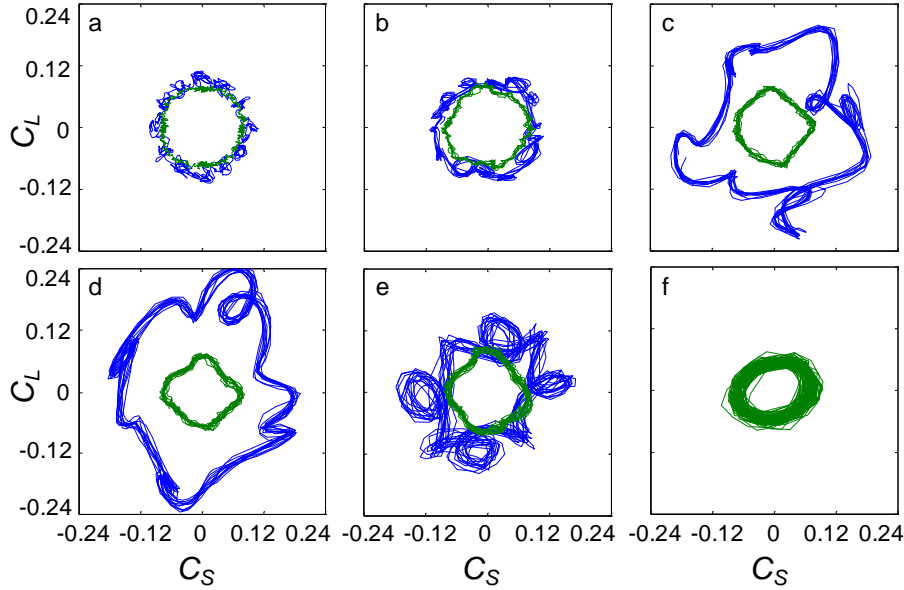


**Figure 9.** Frequency variation of  $C_L$  and  $C_S$  for 1:1 Lissajous rotation (blue) and actuation on a stationary model (green) with effective reduced frequencies at  $k = 0.017$  (a),  $0.086$  (b),  $0.172$  (c),  $0.207$  (d), and  $0.259$  (e), and  $1.434$  (f), acquired over 1 second. Rotation-induced  $C_L$  and  $C_S$  are not acquired for  $k = 1.434$ .

induced force coefficients is much larger than they were at any lower frequency (compare Figure 9f with Figures 9a-e). This approach of implementing spin modulated fluidic actuation at the shedding frequency of the model is investigated further in the wake response in Section V.

Next, the study of the control authority of the fluid actuation on a moving body is tested. Based on the results shown in Figure 9, it is clear that there should be a significant impact on  $C_L$  and  $C_S$  if the fluidic actuation scheme (shown in green) is run in phase or out of phase with the Lissajous 1:1 rotation that induced the aerodynamic loads (shown in blue). In addition, it is also important to check the possible deflection of trajectory ( $x, y, z, \alpha_x, \alpha_y$ , and  $\alpha_z$ ), as well as the changes in the four other coefficients (drag force,  $C_D$ , and roll,  $C_R$ , pitch,  $C_M$ , and yaw,  $C_Y$ , moments), where the moment coefficients are based on the measured moments as  $C = 8M/(8\pi U^2 D^2 L)$ . Initially, the combination of the fluidic actuation shown in Figure 8d and Lissajous rotation in Figure 8a is shown at the representative steady frequency of  $k = 0.017$  in Figure 10. When the actuation and motion are in phase (referred to as the force augmentation case), the corresponding data are shown in red, and when the actuation is run  $180^\circ$  out of phase (force suppression), the data are shown in green, while the unactuated motion response is shown in blue for reference. The nominally zero translational components of the center of the wire mounts on the model are shown on a scale of  $\pm 2\text{mm}$  with streamwise displacement ( $x$ ), and cross-stream displacements ( $y$  and  $z$ ). There are slight variations in  $z$  on the order of  $0.4\text{mm}$ , but for all of these translations there is almost no variation in the motion when actuation is applied, showing that the forces induced in Figures 10g-i are all aerodynamic and not related to inertia effects. The commanded angles of  $3^\circ \alpha_y$  and  $\alpha_z$ ,  $90^\circ$  out of phase are shown in Figures 10e and f, which again have little variation due to actuation, also implying that the moment responses in Figures 10j-l are entirely aerodynamic. There is a slight variation of the roll angle from the commanded value of  $0$  in Figure 10d, but it is less than  $0.4^\circ$  and also is invariant with actuation and therefore is considered negligible. The commanded force suppression (green) and force augmentation (red) are shown with their  $C_S$  and  $C_L$  in Figures 10h and i, respectively and indicate significant control authority over these two coefficients with a suppression of  $60\%$  or an augmentation of  $35\%$ , respectively. It is also important to note that this control negligibly varies the drag seen in Figure 10g, where it is initially a value of  $0.23$  (close to the expected value of  $0.25$ , Hoerner<sup>31</sup>), and the actuation does not significantly increase or decrease  $C_D$  (within the resolution of this time trace of about  $0.02$ ). Likewise, the roll moment, shown in Figure 10j appears to be roughly invariant (with small periodic fluctuations attributed to fluctuations in the roll angle, compare Figure 10j and Figure 10d), and almost no change is induced due to the actuation. Similar to previous studies on this model undergoing a pure pitching motion with no yaw (Lambert et. al<sup>29,30</sup>), the force suppression actuation appears to augment the aerodynamic moments  $C_Y$  and  $C_M$  by about  $50\%$ , and the force augmentation actuation appears to suppress the aerodynamic moments by about  $30\%$ , as seen in Figures 10k and l. This suggests that this actuation could also be applied for control of the aerodynamic moments instead of the

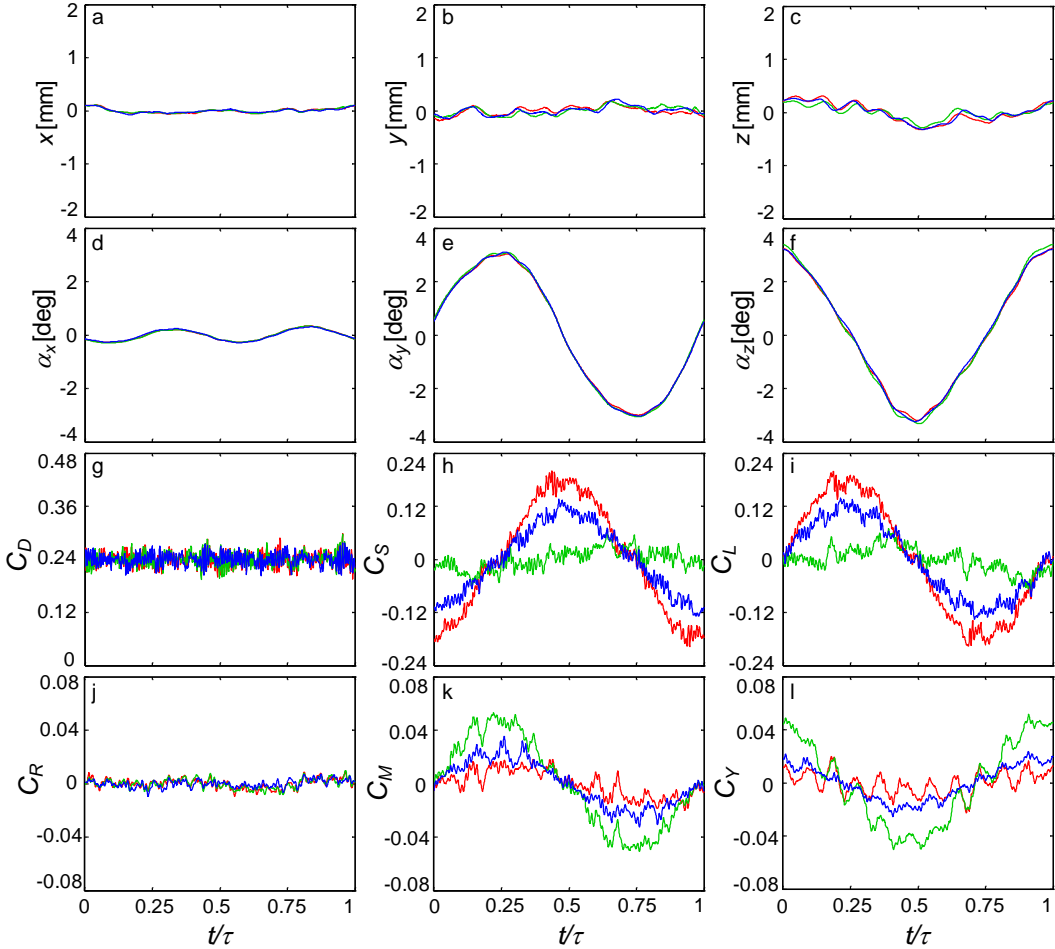


**Figure 10.** Time traces of translational (a – c) and rotational (d – f) components of the model motion, as well as the aerodynamic force (g – i), and moment (j – l) coefficients at  $k = 0.017$ , without (blue) and with actuation for the flow control schemes for the force suppression (green) and augmentation (red) at  $Re_D = 1.8 \cdot 10^5$ . aerodynamic forces, if desired. It is also noted that the motion-resonance frequency is more clearly depicted in the moment traces in Figures 10k and l than in the force traces (compare with Figures 10h and i).

Next, a frequency variation of the force suppression (green) and augmentation (red) control schemes shown in Figure 11 is implemented (similar to that of Figure 9), where the side with lift force variation is shown in Figures 11a,c,e,g, and i and the yaw with pitch moment variation is shown in Figures 11b,d,f,h, and j. Again, the Lissajous rotation without actuation is shown in blue, where the force coefficient traces in Figures 11a,c,e,g and i in blue are the same as the blue traces in Figures 9a-e, plotted on a different scale. The lowest frequency shown in Figures 11a and b shows the same result in Figure 10, with approximately a 60% suppression and 35% augmentation in the forces, respectively, as well as a 30% augmentation and 50% suppression in the moments, respectively. This trend continues with little change in the actuation effect, and small changes in the baseline structure as the reduced frequency is increased to  $k = 0.086$  (Figures 11c and d). It is interesting to note that when the motion is increased to near its spin instability ( $k$  increases to 0.207, see Figures 11e-h), the effect of the actuation *increases* from its initially invariant level that was seen in Figure 9. This shows the effect of the actuation changing with the orientation of the model (and possibly also with the model dynamics) similarly to what was seen previously when this model was varied under pitch and the jet momentum was held constant (Lambert et. al<sup>28</sup>). This new increase in control authority at  $k = 0.207$  yields a force suppression of ~80% and an augmentation of ~100% (Figure 11g), as well as a moment augmentation of ~40% and suppression of ~80% (Figure 11h). It is also interesting to note that the shedding frequency of the model becomes notable in Figures 11e-h, with a response which is approximately nine times faster than the motion in Figures 11e and f, and approximately eight times faster than the motion in Figures 11g and h. As the reduced frequency is increased to past the spin resonance, the force induced by both the flow and the actuation decrease, while the moments induced by the flow and actuation appear to decrease at a slower rate,

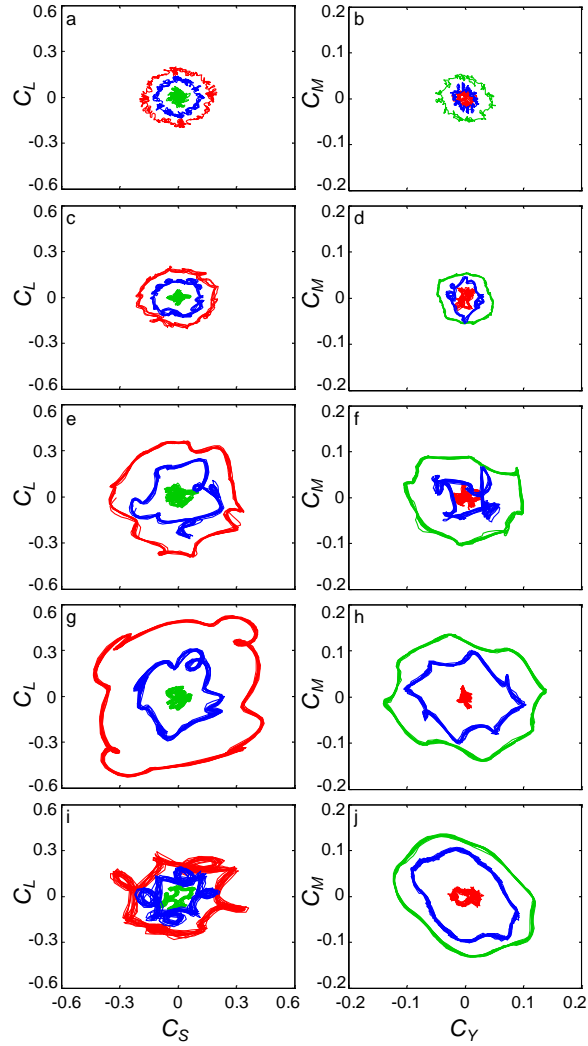


**Figure 11.** Phase plots of lift and side force coefficients (left column) and pitch and yaw moment coefficients (right column) on the model at  $k = 0.017$  (a),  $0.086$  (b),  $0.172$  (c),  $0.207$  (d), and  $0.259$  (e) without (blue) and with the flow control schemes for the force suppression (green) and augmentation (red) at  $Re_D = 1.8 \cdot 10^5$ .

attack in Figure 12. Similar to Figures 9 and 11, the dataset is plotted over a 1 second measurement, which corresponds to 12 periods of motion at  $k = 0.207$ , and this motion is plotted in Figures 12a and b with time. Again, similar to the steady frequency in Figures 10e and f, there is almost no variation in the angle of attack with actuation, and inertia effects of the model can be ignored. Each of the aerodynamic load coefficients is plotted with the angle that induces the most variation (i.e.  $C_L$  and  $C_M$  are plotted with  $\alpha_y$ , and  $C_S$  and  $C_Y$  are plotted with  $\alpha_z$ ). Figure 12c shows  $C_S$  with  $\alpha_z$ , which is similar to the variation of  $C_L$  with  $\alpha_y$  in Figure 12d, with the exception that  $C_S$  increases with negative  $\alpha_z$ , while  $C_L$  increases with positive  $\alpha_y$ . This sign reversal is an artifact of the coordinate system chosen (see Figure 4), where as the model moves in positive pitch ( $+\alpha_y$ ), the lift force increases in the  $+z$  direction, but the side force increases in the  $-y$  direction for the model moving in positive yaw ( $+\alpha_z$ ). Figure 12e shows  $C_Y$  with  $\alpha_z$ , which is also paired with the variation of  $C_M$  with  $\alpha_y$  in Figure 12f. In this case both of the slopes are of the same sense, as the model is unstable (i.e., as the model pitches in  $\alpha_y$  or  $\alpha_z$ , its moment tends to be in the same sense to continue motion in the same direction). Another interesting feature is that the augmentation of force coefficients (Figures 12c and d in red) increases the hysteresis in the  $C_S$  vs.  $\alpha_z$  and  $C_L$  vs.  $\alpha_y$  paths, while suppression of the force coefficients (Figures 12c and d in green) decreases the hysteresis in the force vs. angle path. There is a

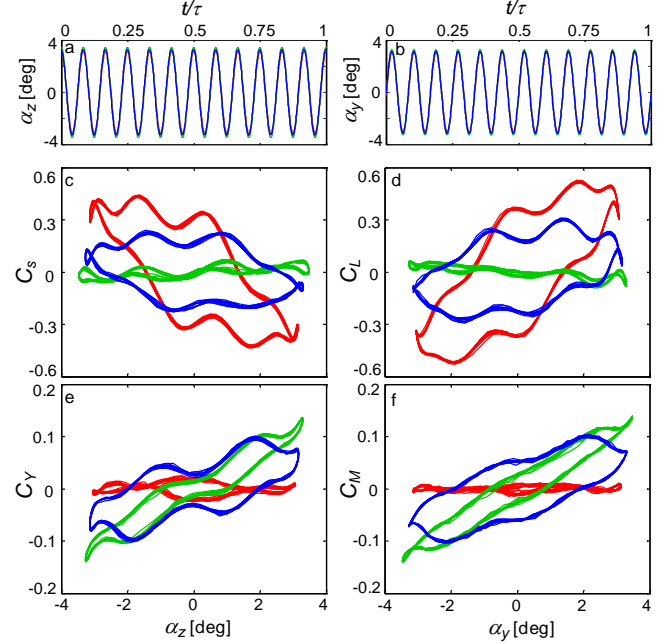


**Figure 12.** Angular motion (*a,b*), as well as angular variation in induced force (*c-d*), and moment (*e-f*) coefficients for  $k=0.207$  without (blue) and with the flow control schemes for the force suppression (green) and augmentation (red) at  $Re_D = 1.8 \cdot 10^5$ .

with the induced moments (Figure 11j) remaining a larger fraction of their steady moments (Figure 11b), when compared to the ratio of the induced forces (Figure 11i) to their representative steady values (Figure 11a).

Upon analyzing the frequency effect on the forces and actuation outcomes, the resonance case of  $k = 0.207$  is selected as the representative *unsteady* aerodynamic frequency for the remainder of the paper. Although Figure 11 gives a detailed description of the forces and moments, and their changes with actuation, it does not include any information about the angles of attack. To study this further the force coefficients and moment coefficients are plotted with their respective angle of

different trend in the moment where although hysteresis in  $C_Y$  vs.  $\alpha_z$  and  $C_M$  vs.  $\alpha_y$  is dramatically reduced with force augmentation (Figures 12e and f in red), the hysteresis in  $C_Y$  vs.  $\alpha_z$  and  $C_M$  vs.  $\alpha_y$  is also slightly decreased in the force suppression actuation (Figures 12e and f in green). It is noted that the hysteresis in force and moment coefficients with angle of attack is expected in unsteady flow, as the wake response lags the model motion. In addition, the shedding frequency further affects all the dynamics seen in Figures 12c-f, where each trace shows a prominent higher frequency attributed to the vortex shedding.

## V. Near Wake Dynamics: Stationary Model with Actuation and Unsteady Pitch/Yaw

This section further investigates the wake response of the representative unsteady 1:1 Lissajous rotation ( $k = 0.207$ ) shown in Figure 12. For the present investigation the wake is characterized with phase-locked PIV measurements over 600 averages and 12 phases throughout the motion cycle. It is noted that the wake response lags the model motion by  $\sim 30^\circ$  at this reduced frequency which is in agreement with both the measured hysteresis in the baseline aerodynamic load measurements in Figure 11 as well as the prior study of phase-lag response at varying  $k$  in pure pitching motion conducted by Lambert et al.<sup>29</sup>. For simplicity, the velocity fields chosen to represent this phase averaged wake response are the four phases where the wake deficit is most horizontally and vertically deflected at  $t/\tau = 0.083, 0.333, 0.583$ , and  $0.833$  (representative phases of  $30^\circ, 120^\circ, 210^\circ$  and  $300^\circ$  with respect to the motion, where  $\tau = 0.083$ s is the time of one motion cycle). The resulting streamwise velocity measured in these four phases is shown in Figures 13a-d for the furthest wake deflections in  $+y$ ,  $-z$ ,  $-y$ , and  $+z$ , respectively. In comparison to the baseline flow in Figure 5a, the effect of the wires is similar, and the wake deficit is smaller than it was when the model was stationary. In addition, the phases show symmetry as expected, where Figure 13a and Figure 13c are similar to mirror images of each other across  $y = 0$ , and Figures 13b and d are also symmetric across  $z = 0$ . For comparison, the streamwise wake behind the model when the sinusoidal modulation fluidic control scheme from Figure 8d is applied on a *stationary* model is shown in the equivalent phases of  $t/\tau = 0.083$  (Figure 13e),  $0.333$  (Figure 13f),  $0.583$  (Figure 13g), and  $.833$  (Figure 13h). There are some key differences to note, as the wake deficit for actuation alone is larger than the wake deficit for motion alone, and the actuation leaves a prominent concave disruption in the wake deficit on the side where the fluidic actuator is activated (see the left side of Figure 13e) However, it is emphasized that these flow fields show that a similar wake to a moving model can be induced on a stationary model with the synthetic jets, demonstrating the control authority that was observed in the forces measured in Section IV (compare Figures 13a and e, b and f, c and g, and d and h, respectively). The cross stream velocity for the motion-induced and actuation-induced flow fields are omitted for brevity as they show similar effects seen in the streamwise velocity analysis.

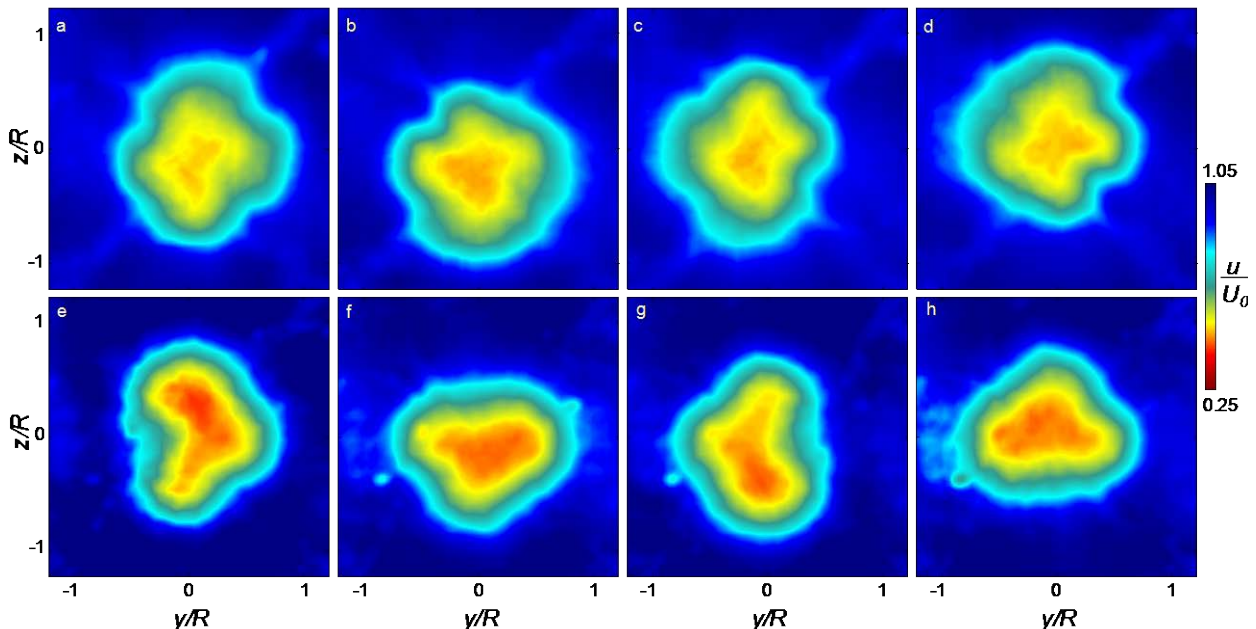


**Figure 13.** Phase-locked contour plots of streamwise velocity component at  $t/\tau = 0.083$ (a,e),  $0.333$  (b,f),  $0.583$  (c,g), and  $0.833$  (d,h) for 1:1 Lissajous rotation without flow control (a-d) and for the equivalent overlapping sinusoidal flow control actuation scheme on a stationary model (e-h, cf. Fig. 8d) at  $Re_D = 1.8 \cdot 10^5$  and  $k = 0.207$ .

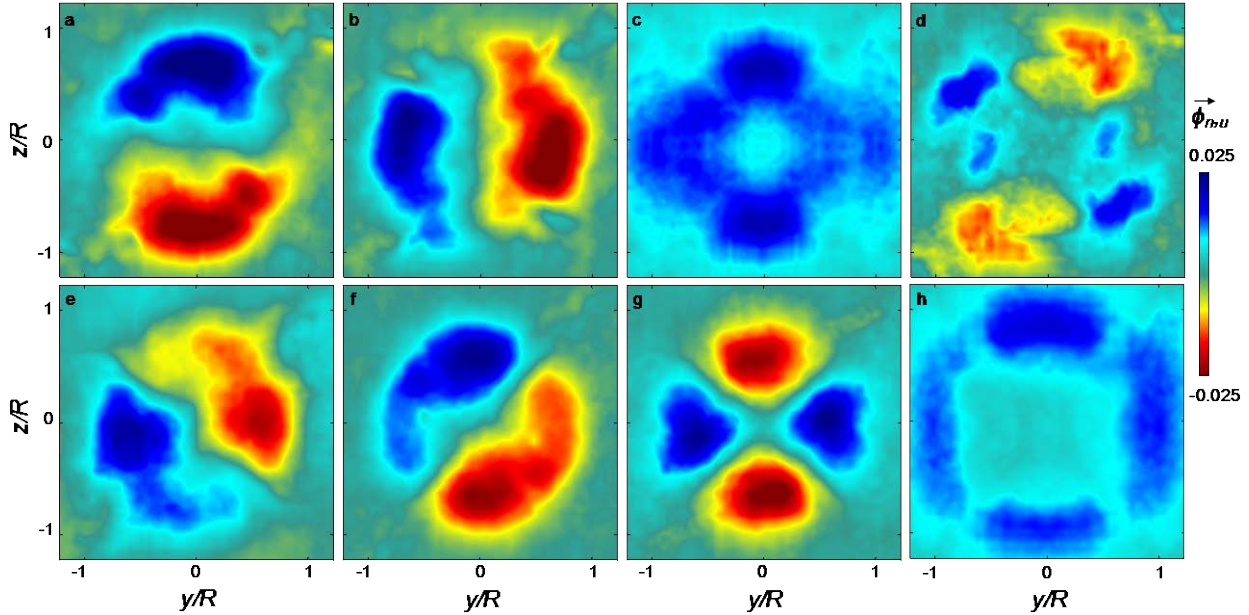


**Figure 14.** Contour plots of the POD modes  $n = 1$  (a,e), 2 (b,f), 3 (c,g), and 4 (d,h) of streamwise velocity  $\vec{\phi}_{n,u}$  for the equivalent Lissajous rotation without flow control (a-d, cf. Fig. 13a-d) and for the overlapping sinusoidal modulation actuation on a stationary model (e-h, cf. Fig. 13e-h).

The wake structure of the Lissajous motion-induced and stationary actuation-induced wakes are analyzed using the same POD mode analysis in Section III for Figures 7 and 8 on a 7,200 image dataset formed by appending 600 instantaneous measurements for 12 phases. The result is shown in Figure 14 with the streamwise velocity modes,  $\vec{\phi}_{n,u}$ , for  $n = 1$  (Figures 14a and e), 2 (Figures 14b and f), 3 (Figures 14c and g), and 4 (Figures 14d and h) of the motion-induced wakes (Figures 13a-d) shown in Figure 14a-d and of the actuation-induced wakes (Figures 13e-h) shown in Figures 14e-h. The first two modes of the motion-induced wakes resemble the first two modes of the baseline wake structure with a 45° rotation (compare Figures 14a and b with Figures 6a and b). This rotation of the primary sign change in the first two streamwise velocity modes shows that the preferential shedding (with highest energy) is now in the direction of yaw alone and the direction of pitch alone. It can be argued that this results from the model longest residence times at its outmost positions where it moves slowest due to the nature of sinusoidal motion. This phenomenon is not realized for the actuation-induced wakes where the first two modes (Figures 14e and f) remain unchanged in orientation and instead only slightly change in structure from the first two modes of the baseline case (Figures 6a and b). A new mode that was not present in the POD modes of the baseline appears as the third strongest mode in the motion-induced wake in Figure 14c which represents the increase or decrease of velocity in the shear layer with respect to the free-stream and central region. It is noteworthy that this mode appears to have a similar shape to the baseline wake deficit on a stationary model (compare Figure 14c with Figure 5a), which suggests that the lack of axisymmetry in this mode may also be attributed to the model geometry. Figure 14d shows the fourth mode in the motion-induced wake which is similar in shape to the third mode of the baseline flow (compare Figure 14d and Figure 6c), with slight variations in structure. The third mode in the actuation-induced wake is shown in Figure 14c, which can be related to the fourth mode of the baseline flow (compare Figure 14g with Figure 6d). The new motion that is induced by the spinning actuation is shown in Figure 14h in the fourth mode, which is similar to the third mode of the motion-induced flow. This suggests that the difference that is observed between the streamwise velocity in the motion-induced wakes of Figures 13a-d and actuation-induced wakes of Figures 13e-h are synonymous with the change in shape of the dynamic modes (Figures 14c and g) as well as the increased energy in this mode when the wake deflection is motion-induced.

The coupling of the motion-induced and actuation-induced wakes in Figure 14 is investigated further in Section VI, and the remainder of this section considers the effect of the spinning actuation of Figures 14e-h on the wake when the frequency is increased to the model shedding frequency of  $k = 1.434$  (commensurate with the forces measured in Figure 9f). However, because the overlapping sinusoidal actuation is applied at a much higher frequency, the phase lag between the wake and the actuation is increased to around ~210°, where this number was derived through the measured actuation force output (Figure 9f) and its corresponding modulation command

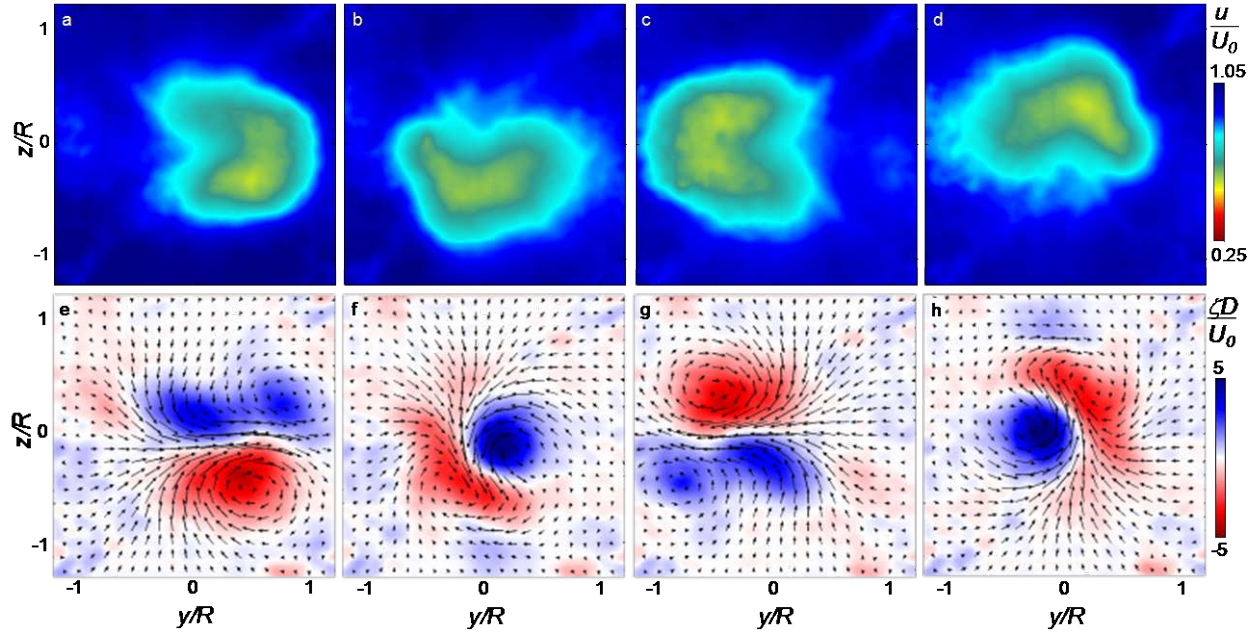


**Figure 15.** Phase-locked contour plots of streamwise velocity (a-d) and the cross stream velocities  $v$  and  $w$  colored by the streamwise vorticity (e-h) at  $t/\tau = 0.583$  (a,e),  $0.833$  (b,f),  $0.083$  (c,g), and  $0.333$  (d,h) for the flow control actuation scheme on a stationary model, modulated at the model shedding frequency,  $k = 1.434$  (83 Hz).

(omitted for brevity). Similar to the dataset in Figure 13, the flow fields are measured through phase-averaged PIV with 600 instantaneous realizations of 12 different phases, of which four are shown in Figure 15. The velocity fields chosen to represent this phase-averaged wake response are the four phases where the wake deficit is most horizontally and vertically deflected at  $t/\tau = 0.583$  (Figures 15a and e),  $0.833$  (Figures 15b and f),  $0.083$  (Figures 15c and g), and  $0.333$  (Figures 15d and h), which are equivalent to phases of  $210^\circ$ ,  $300^\circ$ ,  $30^\circ$  and  $120^\circ$  with respect to the actuation modulation, where  $\tau = 0.012$ s is the time of one motion cycle. The representative phases are shown in Figure 15 with a contour plot of the streamwise velocity,  $u$ , in Figures 15a-d and a quiver plot of the cross-stream velocities,  $v$  and  $w$ , in Figures 15e-h, colored by the streamwise vorticity. Clearly, there are large differences in this flow field from the equivalent actuation-induced flow field at  $k = 0.207$  (Figures 13e-h), as the magnitude of the velocity deficit decreases, and the span of the velocity deficit increases. In addition, the vertical deflection of the velocity deficit region is similar to the lower frequency (compare Figures 15b and d with Figures 13b and d), but the horizontal deflection is much larger (compare Figures 15a and c with Figures 13b and d). This increased deflection in the horizontal direction is investigated further in the cross-stream velocities in Figures 15e-h, where in Figures 15e and g, a third significant vortex appears in the flow, when the streamwise velocity wake deficit is deflected horizontally. If this vortex were removed the magnitude of the streamwise vorticity in all of the phases would look similar to each other (compare the two vortices in Figures 15f and h with the primary two vortices in Figures 15e and g). This suggests that this extra shedding vortex which could, in principle, have been formed at any angle in this field of view, due to its axisymmetry, is maintained in the yawing direction, perhaps due to slight imbalances in the strength of the actuation. This result implies that timing the fluidic actuation to the shedding frequency of the wake even when the actuation is axisymmetric (has equal commands in the pitching and yawing directions) can maintain the shedding instability in a preferential pitch-yaw direction over a much larger time scale, suggesting that with the implementation of the right sensors for detecting the flow instability these fluidic actuators may be implemented for *control* of the vortex shedding.

The structure of the wake when actuation is triggered at the shedding frequency is also investigated further by concatenating the all of the instantaneous realizations of the 12 phase averaged data set in Figure 15 to calculate the POD modes  $\vec{\varphi}_n$  which are shown in Figure 16 (analogous to the streamwise POD modes shown in Figure 14). The streamwise velocity subset of the POD modes  $\vec{\varphi}_{n,u}$  are shown in Figure 16 with  $n = 1$  (Figure 16a),  $2$  (Figure 16b),  $3$  (Figure 16c), and  $4$  (Figure 16d). The first two modes (Figures 16a-b) represent a paired two-fold symmetry, similar to actuation at the lower frequency (Figures 14e-f), without a bias along  $45^\circ$  from the top, instead being biased in the pitch and yaw directions. These structures, although induced on a stationary model, clearly resemble those of the

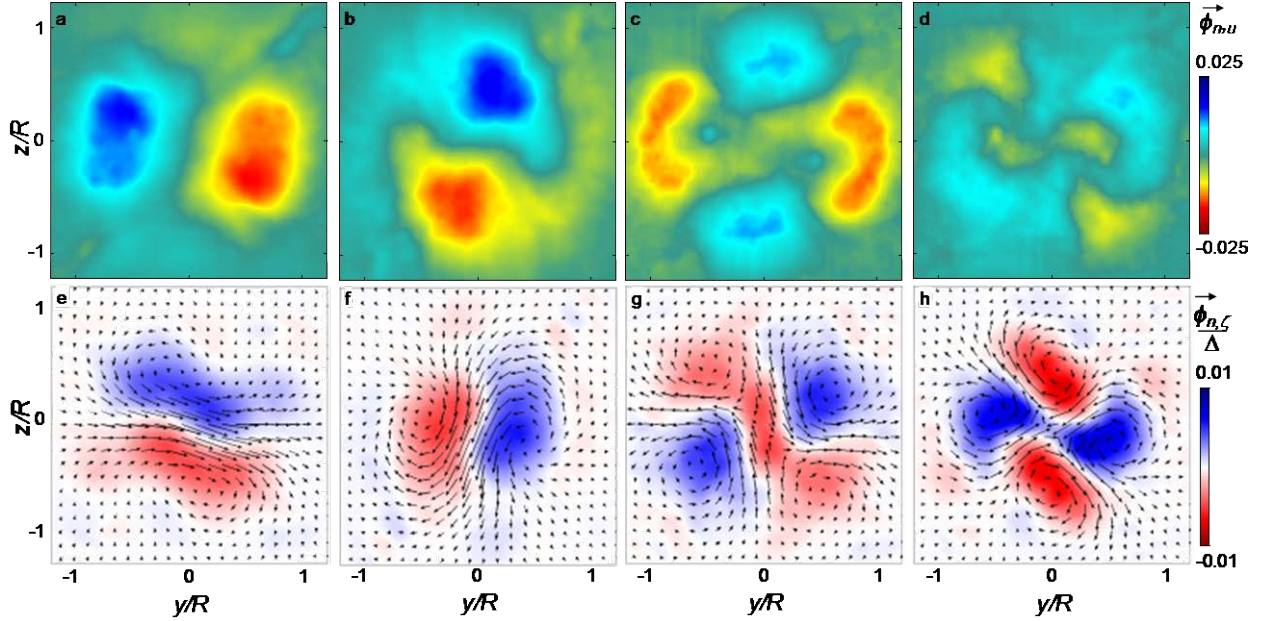


**Figure 16.** Contour plots of the POD modes  $n = 1$  (a-d),  $2$  (b-f),  $3$  (c-g), and  $4$  (d-h) of streamwise velocity modes  $\vec{\phi}_{n,u}$  (a-d), and the cross-stream velocity modes  $\vec{\phi}_{n,v}$  and  $\vec{\phi}_{n,w}$  (e-h) colored by their streamwise vorticity,  $\vec{\phi}_{n,\zeta}$ , for the flow control actuation scheme on a stationary model shown in Fig. 15.

motion-induced wake of Figures 14a-b. Figure 16c and d are approximately similar to the modes with four-fold symmetry of baseline wake (compare Figures 16c-d with Figures 6c-d), but have a more significantly diffused and spread out structure than observed in the stationary model. It is also interesting to note that the mode depicted in Figure 14h corresponding to the shear layer dynamics induced by the actuation at  $k = 0.207$  is not present in the first four modes. The commensurate first four modes of the cross-stream velocity are shown in Figures 16e-h. The addition of the new vortex in the yaw direction in Figures 15e and g is reflected in the fact that the first two modes in Figures 16e and f are now no longer rotated pairs. The mode that corresponds to shedding in the yawing direction has the secondary vortex encompassed in its mode (which is also the mode that has the most energy contribution). The second, third, and fourth modes however are more diffuse versions of the same structures observed in the baseline flow modes with slight changes in structure (compare Figures 16f-h with Figures 7f-h). These results show that the fluidic actuators in this scenario does not only excite the highest energy mode, but changes its shape as well.

## VI. Dynamic Model: Controlled Near-Wake Structure

This section further investigates the near wake effects of the fluidic control schemes for force suppression and augmentation on a body undergoing 1:1 Lissajous rotation at  $k = 0.207$ , synonymous with the forces in Section IV (see Figure 12). The application of both of these actuations are shown in Figure 17, with the force suppression in Figures 17a-d and the force augmentation in Figures 17e-h. This wake is characterized with phase-locked PIV measurements in the same fashion as formerly shown in Figure 13 with representative streamwise velocity fields,  $u$ , at  $t/\tau = 0.083$  (Figures 17a and e),  $0.333$  (Figures 17b and f),  $0.583$  (Figures 17c and g), and  $0.833$  (Figures 17d and h), which are representative phases of  $30^\circ$ ,  $120^\circ$ ,  $210^\circ$ , and  $300^\circ$  with respect to the motion, where  $\tau = 0.083$ s. The force augmentation actuation shown in Figures 17a-d is the combined effect of the Lissajous 1:1 rotation induced wake (Figures 13a-d) and the actuation-induced wake control scheme shown in Figures 13e-h run synchronously and out of phase with each other, in order to have the opposing effects. When the force suppression scheme is applied, wake responds to the effect of activation of the right jet (Figure 17a), the streamwise velocity wake deficit region develops a similar structure to when this actuation was applied on a stationary body (compare Figures 17a and Figure 13c, noting the actuation in Figures 13e-h is  $180^\circ$  out of phase with the actuation in Figures 17a-d). The main difference between Figures 17a-d and Figures 13e-h is that the vertical and horizontal extent of the wake deflection is altered and reduced (compare Figures 17a and c showing less horizontal deflection and slightly more vertical deflection to Figures 13g and e, and likewise compare Figures 17b and d to Figures 13f and h). With this fluidic actuation, the wake deficit region now is concave in the direction the wake would have deflected without actuation, minimizing the motion induced deflection, and increasing the magnitude of the wake deficit to the levels

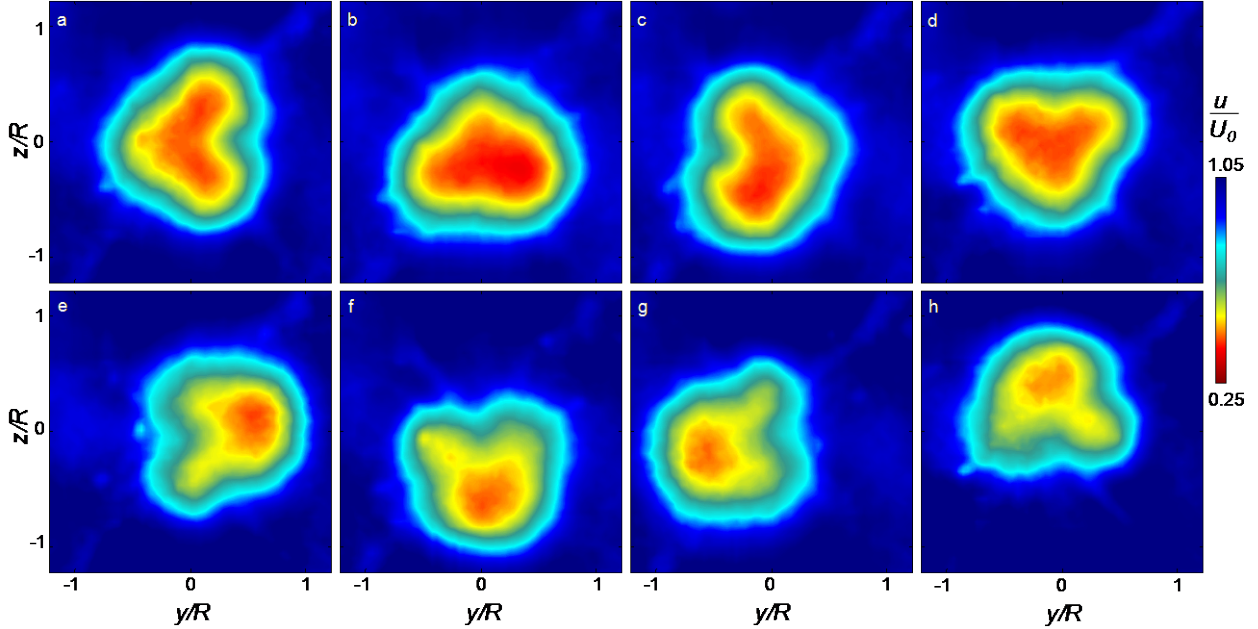


**Figure 17.** Phase-locked contour plots of streamwise velocity component at  $t/\tau = 0.083(a,e)$ ,  $0.333(b,f)$ ,  $0.583(c,g)$ , and  $0.833(d,h)$  for the force suppression (a-d) and the force augmentation (e-h) flow control schemes at  $Re_D = 1.8 \cdot 10^5$  and  $k = 0.207$ .

similar to the baseline flow (compare Figures 17a-d with Figure 5a). Figures 17e-h shows the force augmentation with fluidic actuation, where the same flow control pattern of Figures 13e-h is applied as before on the dynamic wake, similar to Figures 17a-d, except that the actuation is in phase with the motion-induced response. Figure 17e shows an increased deflection of the deficit in  $u$  to the centerlines of  $y = 0$  and  $z = 0$ . It is noted that the wake response to this actuation in Figures 17e-h is tilted in a counter-clockwise direction compared to the nominally vertical and horizontal phases seen before in Figures 13a-h, showing that the wake lags the model development by slightly more than  $30^\circ$  in phase assumed previously (i.e., if the phase-averaged  $u$  fields were measured at a slightly larger phase difference, the wake would move slightly more clockwise in all of Figures 17e-h). This increase in phase lag is commensurate with the increase in force hysteresis measured in the force augmentation case shown in red in Figures 12c-d relative to the unactuated case shown in blue. Figures 12c-d also showed a decrease in phase lag in the force suppression actuation (shown in green trace), which is also an explanation of why the wake in Figures 17a-d moves vertically between the assumed horizontal phases Figures 17a and c, and moves horizontally in Figures 17b and d. It is important to emphasize that these flow control schemes not only decoupled / enhanced the coupling of the wake response (shown in Figure 17), but they also consequently decoupled / enhanced the coupling of the aerodynamic forces from the model motion (as shown earlier in Figures 12c-d), which shows substantial control authority for disturbance rejection of wake-induced forces that can potentially be implemented on this model in flight for stabilization or steering.

The unsteady wake structures of the force suppression and augmentation flow control schemes applied in Figure 17 for the model undergoing Lissajous rotation are analyzed using the same POD mode analysis used in Section V for Figure 14 and shown in Figure 18. The streamwise velocity modes,  $\vec{\varphi}_{n,u}$ , for  $n = 1$  (Figures 18a and e), 2 (Figures 18b and f), 3 (Figures 18c and g), and 4 (Figures 18d and h) are shown for the force-suppressed wakes of Figures 17a-d and of the actuation-induced wakes in Figures 17e-h shown in Figures 18e-h. For both the force suppress and the force suppression cases, the first two modes (Figures 18a-b and Figures 18e-f) have the signature two-fold symmetry seen before in the baseline flow, actuation alone, and motion alone cases (Figures 6a-b, Figures 13a-b, and Figures 13e-f, respectively). However, it is interesting to note that the tilting angle of the actuated cases is inverted, where the first two suppression modes are tilted counterclockwise from the baseline modes (compare Figures 18a-b with Figures 13a-b) and the first two augmentation modes are tilted in the opposite, clockwise, direction (compare Figures 18e-f with Figures 13a-b). These modes in essence show that the suppression and augmentation actuators have the *opposite* effect on the baseline flow induced by dynamic actuation spin, and it is also noteworthy that the force suppression modes are altered to closer resemble the baseline modes shown in Figures 6a-b. Effectively, it suggests that this actuation transforms the structure of the flow of this dynamic body to

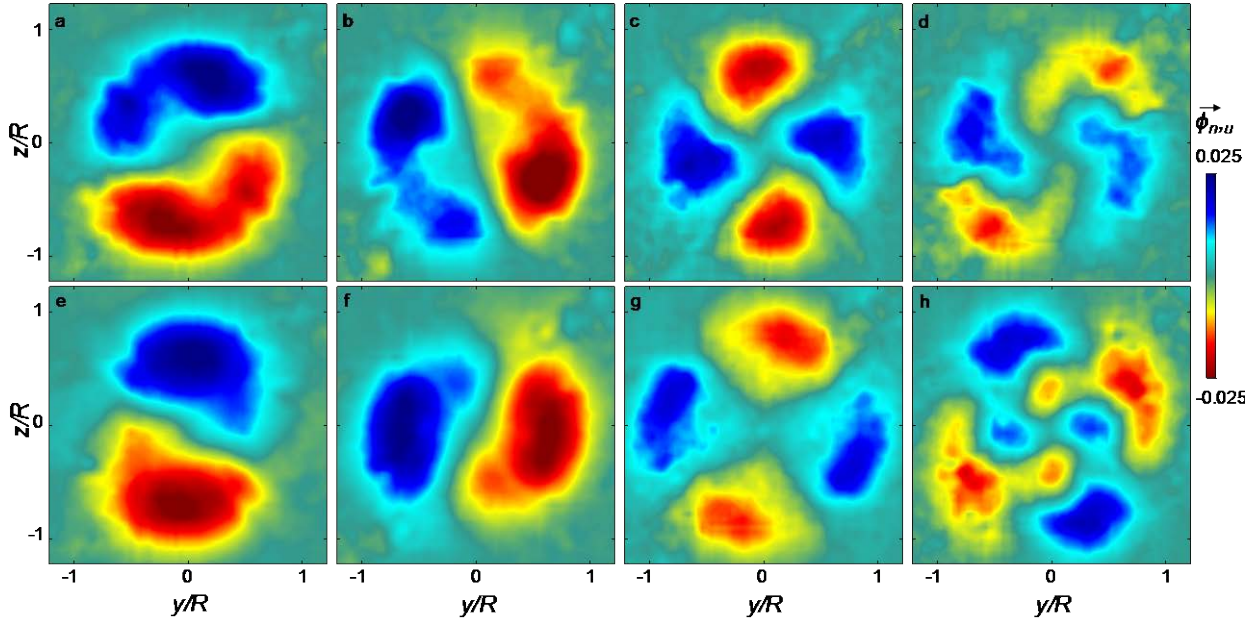


**Figure 18.** Contour plots of the POD modes  $n = 1$  (a,e), 2 (b,f), 3 (c,g), and 4 (d,h) of streamwise velocity  $\vec{\phi}_{n,u}$  for the force suppression (a-d) and force augmentation (e-h) flow control of Figure 17.

a structure that is reminiscent of the flow on a static body, and is decoupling the wake from the model motion. Following the same analysis, the coupling of the flow response to the motion is enhanced with model actuation. The third and fourth mode of the suppression actuation are similar to the baseline flow as well (compare Figures 18c and d with Figures 6d and c). The respective third and fourth mode of the augmented flow show an increased tilting angle and are further spread out in the radial direction than the suppressed mode (compare Figures 18c-d with Figures 18g-h). These modes also show a progression of the wake coupling from Figure 18d (decoupled) to Figure 14d (no actuation) to figure 18h (increased coupling), as seen in the suppressed mode in Figure 18d, where the structure spreads out and new wake features develop closer to the center.

The combined result of the time development of all of the wake studies performed in Section V and VI are compared in Figure 19 through a trace of the vertical centerline (i.e.  $z = 0$  with varying  $y$ ) of all twelve phase averaged PIV flow fields which are equally spaced phases in time. All of these  $y-t$  data sets are taken with a frequency of actuation or motion set to  $k = 0.207$  at a  $Re_D = 1.8 \cdot 10^5$  at  $x/D = 1.9$  (i.e., one diameter downstream of the aft end of the model). The measured velocities  $u$ ,  $v$ , and  $w$ , are shown in Figures 19a-e, 19f-j, and 19k-o, respectively, and the measured streamwise vorticity,  $\zeta$ , is shown in Figures 19p-t. The wake responses of a stationary model without actuation (seen previously in Figure 5) and with actuation (seen previously in Figures 13e-h) are shown in Figures 19a,f,k, and p, and Figures 19b,g,l, and q, respectively. The wake responses of a dynamic 1:1 Lissajous rotating model are shown without actuation (Figures 19c,h,m and r), with force suppression actuation (Figures 19d,i,n, and s), and with force augmentation actuation (Figures 19e,j,o, and t). It is noted that the four phases that were shown previously to represent the wake flow field occur at  $t/\tau = 0.083, 0.333, 0.583$ , and  $0.833$  in these data. The analysis is focused on two aspects of the applied flow control: *i*) the appropriate actuation on a stationary model (Figures 19b,g,l, and q) can successfully mimic the effect dynamic motion has in the wake downstream of an axisymmetric bluff body, and *ii*) timed fluidic actuation on a dynamic body can significantly decouple the wake response from the motion response, or alternatively enhance this coupling. These effects are clearly demonstrated in  $u$ , where the extent of the time development of the wake deficit on a stationary model resembles the wake deflection from the dynamic model (compare Figures 19b and c). If the fluidic actuation in Figure 19b is applied out of phase with the model rotation in Figure 19c, the wake becomes decoupled and resembles the wake of a static body without actuation (compare Figures 19a and d), and if the fluidic actuation is in phase (Figure 19e), the deflection of the velocity deficit is larger with the model motion (i.e., the coupling is enhanced). The cross-stream velocity,  $v$ , shown in Figures 19f-j which is in-line with the actuators that effect the horizontal centerline of the wake shows the largest changes when actuation is present (in Figures 19g, i and j) which dominate the motion-induced wake (Figure 19h), even for the force suppression case which causes a slight increase in the deflection of  $v$ , but is still significantly smaller than the reduction of the deflection in  $u$ . The force augmentation introduces the largest values of  $v$  (see Figure 19j), which is even larger than the effect of  $v$  in the

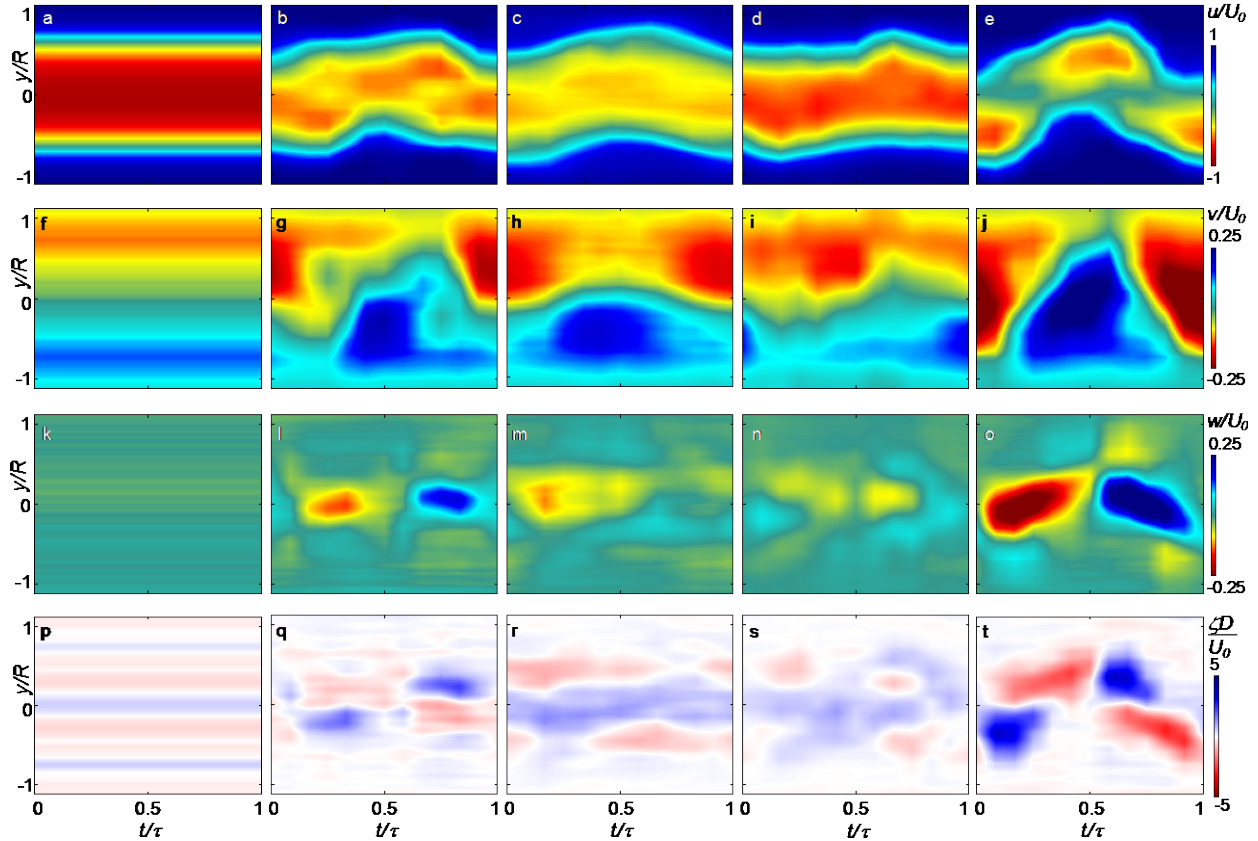


**Figure 19.**  $y$ - $t$  diagrams of the velocities,  $u$  (a-e),  $v$  (f-j), and  $w$  (k-o), and the vorticity,  $\zeta$  (p-t), along the horizontal symmetry line ( $z = 0$ ) at  $x/D = 1.9$ , depicting: the stationary model without (a,f,k,p), and with (b,g,l,q) spinning sinusoidal modulated actuation, and the model moving with 1:1 Lissajous rotation at  $3^\circ$  for unactuated (c,h,m,r), suppression (d,i,n,s), and augmentation (e,j,o,t) flow control, at  $k = 0.207$  and  $Re_D = 1.8 \cdot 10^5$ .

actuation alone (Figure 19g) and motion alone (Figure 19h) combined. The cross-stream velocity,  $w$ , shown in Figures 19k-o has the smallest variations of all the velocity flow fields, and shows slight deviations with actuation (compare Figures 19k and l) or with motion (compare Figures 19k and m), that seem to slightly decrease with force suppression (Figure 19n) or to significantly enhance with force augmentation (Figure 19o). The streamwise vorticity,  $\zeta$ , is shown in Figures 19p-t which initially has a band structure commensurate with the weak eight lobe structure seen before in Figure 6b shown in Figure 19p. Upon actuation (Figure 19q),  $\zeta$  changes into a two band structure which switches signs when actuation is effecting the wake ( $t/\tau = 0.083$  and  $0.583$ , respectively). This structure is far less organized when the model is rotating without actuation (Figure 19r) where there appears to be a 3 band structure with the outer band severed at the extremes of motion. For the force suppression actuation scheme shown in Figure 19s,  $\zeta$  changes into a predominant counterclockwise field with little structure, and alternatively with force augmentation actuation the two band structure shown with actuation is reintroduced, however the opposite clockwise  $\zeta$  lobes are the dominant features (compare Figures 19t and q).

The final result summarizes the effects of all the actuation and rotational motion studied in this paper through tracking the centroid of the respective wake deficit regions (which are defined by having a velocity magnitude of  $|\vec{V}| < 0.8U_0$ ). This centroid is initially measured in length as  $y_c$  and  $z_c$ , and is converted into a wake angle with respect to the center of model motion:

$$\theta_y = \text{atan}\left(\frac{y_c}{1.9D}\right), \quad \theta_z = \text{atan}\left(\frac{z_c}{1.9D}\right)$$

where  $1.9D$  is the streamwise position of the wake relative to where the model pivots as it rotates. Figure 20 shows these two representative angles of the velocity deficit region plotted against each other for the model undergoing Lissajous rotation (Figure 20a, in closed symbols), and the stationary model with applied actuation (Figure 20b in open symbols). The moving model without actuation at  $k = 0.207$  is shown in blue in Figure 20a, and the

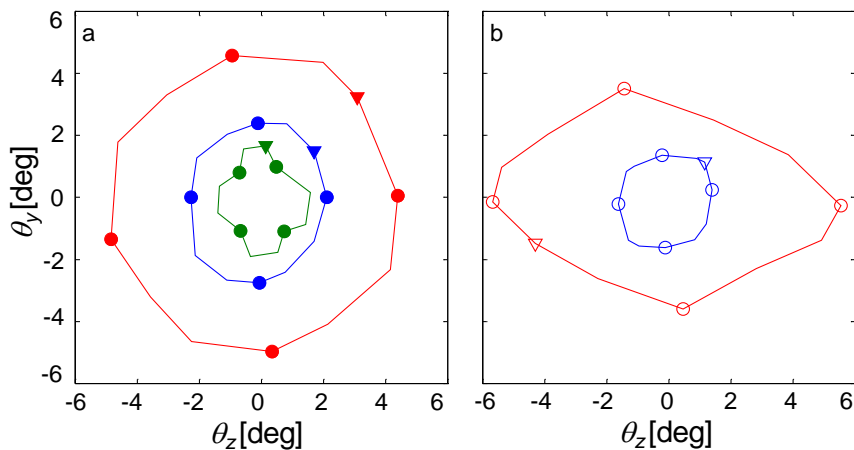


**Figure 20.** Centroid of the wake region defined by  $|\vec{V}| < 0.8U_0$  calculated at 12 phase points, with the starting phase for a dynamically moving model at  $k=0.207$  (a) without actuation (blue), and with force suppression (green) and augmentation (red) actuation, along with a stationary model (b) with sinusoidal modulated actuation at  $k = 0.207$  (blue) and  $k = 1.434$  (red). The phases in circles mark the phases of velocity fields previously shown in Figure 13, 15, and 17.

augmentation actuation (red), the wake deflection is increased by ~80% (from an  $\sim 2.5^\circ$  to  $\sim 4.5^\circ$  radius of deflection) of the unactuated value, and likewise the suppression actuation reduces the wake deflection by ~40% (from an  $\sim 2.5^\circ$  to  $\sim 1.5^\circ$  radius of deflection) of the baseline value. The change in phase response of the augmented wake observed in Figure 17 is clearly present in Figure 20a as the red curve is tilted counterclockwise, and in addition the structure of the suppressed wake is not circular, where the actuation appears to have more of an effect at the points shown in circles (which is also when the maximum single jet actuation effect occurred in the wake, as opposed to a combined jet effect). However, these results still demonstrate substantial control authority, similar to what was seen in the lift and side forces in Figure 12. Figure 20b shows the deflection of the wake of the stationary model with the spinning actuation at  $k = 0.207$  (blue) and  $k = 1.434$  (red). These data show that the wake of a stationary model can be effectively controlled to a similar level as a dynamic model that is pitching and yawing out of phase (in this case, the actuation induced a  $\sim 1.5^\circ$  radius of deflection in the wake, which was 60% of the dynamic model's  $\sim 2.5^\circ$ ). The red trace in Figure 20b shows the coupling of the fluidic actuation to the natural shedding frequency (commensurate with Figure 15), where the phase lag of the actuation onset is approximately  $210^\circ$  from the first PIV phase presented. This result shows that in addition to controlling forces induced by the body dynamics, these actuators have the potential to control forces induced by the natural shedding frequency as well, which can possibly be implemented to increase steering control authority of airborne bodies in future work.

## VII. Conclusions

The unsteady aerodynamic loads on a moving axisymmetric bluff body are controlled in wind tunnel experiments by modification of the coupling between the cross flow over the body and the near wake using an azimuthal array of four hybrid synthetic jet actuators around the aft end. The actuation leads to partial, segmented attachment of the nominally axisymmetric separated shear layer of the base flow leading to a controlled wake asymmetry and concomitant reaction of the aerodynamic loads. The model that is supported by eight servo-controlled wires and can be programmed to execute time-dependent, six degrees of freedom motion along a prescribed trajectory under closed-loop control using feedback from a motion analysis system. In the present investigations the model moves in combined pitch/yaw over a range of reduced frequencies designed to mimic the natural unstable motion of a similar airborne platform in the absence of roll. The flow evolution is characterized using high-resolution SPIV measurements within a  $y$ - $z$  plane that is normal to the geometric centerline,  $x/D = 1$  downstream of the model's aft end ( $1.3 < y/R, z/R < 1.3$ ). Enhancement and suppression of motion-induced aerodynamic loads on the model are each investigated using coupled force and moment measurements and stereo particle image velocimetry in the near wake at reduced frequencies of up to  $k = 0.26$ .

The control effectiveness of the actuation on the near wake is demonstrated on a stationary model. Time-dependent azimuthal actuation is effected using harmonic modulation of the resonance waveform of each of the four

application of force suppression and augmentation actuators are shown in green and red, respectively. In addition, there are representative markers in each data trace: the triangle represents when the Lissajous motion and sinusoidal modulation actuation schemes (shown in Figures 8a and d, respectively) are first applied in time, and the circles mark phases that were used to illustrate the corresponding PIV flow fields of the actuation (i.e., the wake deflections shown in blue circles in 20a correspond to the phase averaged flow fields in Figures 13a-d). Figure 20a clearly shows that upon

independent synthetic jet modules over a broad range of reduced frequencies  $0.017 < k < 1.434$ . It is shown that the actuation can alter the evolution of the aerodynamic loads yielding significant changes in the side and lift forces, and pitch and yaw moments, with negligible effect on the drag or roll moment. Furthermore, it is demonstrated that the structure of the near wake of the *stationary model* in the presence of actuation is similar to the wake of the *moving model* in a “natural” unstable pitch/yaw motion with an amplitude of up to  $3^\circ$ . While at a lower reduced frequency, the aerodynamic loads induced by the actuation are nearly identical to the corresponding aerodynamic loads of the uncontrolled flow over the dynamic pitch/yaw body, the control authority at a fixed actuation level diminishes somewhat as  $k$  increases to 0.207 (its measured pitch/yaw resonance frequency), and then the control authority increases again as  $k$  is increased to 0.259. In addition, the actuation on the stationary model is applied at its vortex shedding frequency ( $k = 1.43$ ,  $St_D = 0.234$ ) leading to strong coupling as manifested by a change of the energy distribution in the wake which is evidenced by alteration of the flow’s POD modes.

Two flow control strategies are demonstrated when the model is undergoing combined pitch/yaw motions. The first strategy focuses on decoupling the wake response from the model motion, and is designed to render the wake response invariant and equivalent to the wake of a nominally static model. The second strategy intensifies the response of the wake to the prescribed motion of the body to mimic larger angular pitch/yaw deflection. These strategies were applied at reduced frequencies within the range  $0.017 < k < 0.259$  and demonstrated up to 75% reduction or 100% augmentation of the motion-induced side and lift forces *without an increase in drag* (within the resolution of the measurements). Alternatively, the actuation can lead to variation of the motion-induced pitch and yaw moments with resulting in 80% reduction or 40% augmentation without affecting the roll moment. Measurement of the velocity distribution in the near wake show that when the actuation to decouple the wake from the model motion is applied, the first four POD modes become similar to the modes of the stationary model in the absence of actuation, even though the body is still moving, and there is a 40% suppression in the motion of the wake’s centroid. Alternatively, when the actuation enhances the coupling to the wake, the POD modes are extended radially, commensurate with the increase in wake deflection, and there is a 80% augmentation in the motion of the wake’s centroid. The present investigations shows that the effects of the actuation on the near wake of the body are comparable to the effects of its baseline unstable pitch/yaw motion and therefore can be used to induce aerodynamic loads that cancel or enhance the baseline aerodynamic loads to effect dynamic steering and stabilization.

## Acknowledgment

This work has been supported by Georgia Tech and the Army Research Office.

## References

- <sup>1</sup>Wu, J.-Z., Lu, X.-Y., Denny, A. G., Fan, M., and Wu, J.-M., “Post Stall Flow Control on an Airfoil by Local Unsteady Forcing,” *Journal of Fluid Mechanics*, Vol. 371, 21-58, 1998.
- <sup>2</sup>Erk, P. P., “Separation Control on a Post-stall Airfoil using Acoustically Generated Perturbations”, PhD Thesis, Tech. Univ. Berlin, Germany, 1997.
- <sup>3</sup>Smith, D. R., Amitay, M., Kibens, V., Parekh, D., and Glezer, A., “Modification of Lifting Body Aerodynamics Using Synthetic Jet Actuators”, *AIAA Paper* 1998-0209, 1998.
- <sup>4</sup>Amitay, M., Smith, D. R., Kibens, V., Parekh, D. E., and Glezer, A., “Aerodynamic Flow Control over an Unconventional Airfoil Using Synthetic Jet Actuators”, *AIAA J.*, Vol. 39, 2001, pp. 361-370.
- <sup>5</sup>Honohan, A. M., Amitay, M., and Glezer, A., “Aerodynamic Control using Synthetic Jets”, *AIAA Paper* 2000-2401, 2000.
- <sup>6</sup>Glezer, A., Amitay, M., and Honohan, A. “Aspects of Low- and High-Frequency Actuation for Aerodynamic Flow Control,” *AIAA Journal*, Vol. 43, 1501-1511, 2005.
- <sup>7</sup>Newman, B.G., “The Deflexion of Plane Jets by Adjacent Boundaries-Coanda Effect”, *Boundary Layer and Flow Control Principles and Applications*, Vol. 1, 1961, pp. 232-264.
- <sup>8</sup>Englar, Robert J., “Circulation Control Pneumatic Aerodynamics: Blown Force and Moment Augmentation and Modification; Past, Present, & Future”, *AIAA Paper* 2000-2541.
- <sup>9</sup>Nagib, H. M., Reisenthel, P. H., and Koga, D. J. “On the Dynamical Scaling of Forced Unsteady Flows”, *AIAA Paper* 1985-0553, 1985.
- <sup>10</sup>Lo, K. P., Elkins, C. J., Eaton, J. K., “Separation Control in a Conical Diffuser with an Annular Inlet: Center Body Wake Separation”, *Exp. Fluids*, Vol 53, 2012, pp 1317-1326.
- <sup>11</sup>Freund, J. B., Mungal, M. G., “Drag and Wake Modification of Axisymmetric Bluff Bodies Using Coanda Blowing”, *J. Aircraft*, Vol. 31, 1994, pp. 572-578
- <sup>12</sup>Rinehart, C., McMichael, J. M., and Glezer, A., “Transitory Flow and Force Development on a Body of Revolution Using Synthetic Jet Actuation”, *AIAA Paper* 2003-0618, 2003.
- <sup>13</sup>Rinehart, C., “Aerodynamic Forces Induced by Controlled Transitory Flow on a Body of Revolution”, Ph. D. Thesis, Georgia Institute of Technology, 2011.

- <sup>14</sup>McMichael, J., Lovas, A., Plostins, P., Sahu J., Brown, G., and Glezer, A., "Microadaptive Flow Control Applied to a Spinning Projectile", *AIAA Paper* 2004-2512, 2004.
- <sup>15</sup>Corke, T. C., Tillotson, D., Patel, M. P., Su, W. J., Toldeo, W., "Radius Flow Vectoring for Projectile Drag and Steering Control Using Plasma Actuators", *AIAA Paper* 2008-3769, 2008.
- <sup>16</sup>Abramson, P., Vukasinovic, B., and Glezer, A., "Direct Measurements of Controlled Aerodynamic Forces on a Wire-suspended Axisymmetric Body", *Exp. Fluids*, Vol. 50, 2011, pp. 1711-1725.
- <sup>17</sup>Abramson, P., Vukasinovic, B., and Glezer, A., Fluidic Control of Aerodynamic Forces on a Bluff Body of Revolution, *AIAA J.*, Vol. 50, pp.832-843, 2012.
- <sup>18</sup>Lambert, T. J., Vukasinovic, B., and Glezer, A. "Yaw Control of a Moving Axisymmetric Body using Synthetic Jets", *AIAA Paper* 2013-0106, 2013.
- <sup>19</sup>Nicolaides, J. D., "A History of Ordnance Flight Dynamics", *AIAA Paper* 70-533, 1970.
- <sup>20</sup>Murphy, C. H., "Symmetric Missile Dynamic Instabilities", *AIAA J. Guidance and Control*, Vol. 4, No. 5, 80-0320R, 1980.
- <sup>21</sup>Price Jr., D. A., "Sources, Mechanisms, and Control of Roll Resonance Phenomena for Sounding Rockets.", *AIAA J. Spacecraft*, **4**, No. 11, 1516-1521, 1967.
- <sup>22</sup>Murphy, C. H., "Some Special Cases of Spin-Yaw Lock In", US Army Ballistic Research Laboratory, BRL-MR-3609, 1987.
- <sup>23</sup>Barrett, R. M., Lee, G. M., "Design and Testing of Piezoelectric Flight Control Actuators for Hard Launch Munitions," *Proc. SPIE* 5390, Smart Structures and Materials 2004: Smart Structures and Integrated Systems, 459, 2004.
- <sup>24</sup>Sahu, J., "Time-Accurate Computations of Free-Flight Aerodynamics of a Spinning Projectile with and without Flow Control", *AIAA Paper*, 2006-6006.
- <sup>25</sup>Ollerenshaw, D., Costello, M., "Model Predictive Control of a Direct Fire Projectile Equipped with Canards," *Journal of Dynamic Systems, Measurement, and Control*, Vol. 130, 2008.
- <sup>26</sup>Ollerenshaw, D., Costello, M., "Simplified Projectile Swerve Solution for General Control Inputs," *Journal of Guidance, Control, and Dynamics*, Vol. 31, 1259-1265, 2008.
- <sup>27</sup>Higuchi, H., Van Langen, P., Sawada, H., Timney, C. E., "Axial Flow Over a Blunt Circular Cylinder With and Without Shear Layer Reattachment", *J. Fluids Struct.*, Vol. 22, 1996, pp. 949-959.
- <sup>28</sup>Lambert, T. J., Vukasinovic, B., and Glezer, A. "Active Decoupling of the Axisymmetric Body Wake Response to a Pitching Motion", *J. Fluids Struct.*, Vol. 59, 2015, pp. 129-145.
- <sup>29</sup>Lambert, T. J., Vukasinovic, B., and Glezer, A. "Aerodynamic Flow Control of a Moving Axisymmetric Bluff Body", *AIAA Paper* 2014-0932, 2014.
- <sup>30</sup>Lambert, T. J., Vukasinovic, B., and Glezer, A. "Unsteady Aerodynamic Loads Effected by Flow Control on a Moving Axisymmetric Bluff Body", *AIAA Paper* 2015-0827, 2015.
- <sup>31</sup>Hoerner, S. F., *Fluid-Dynamic Drag*, Hoerner Fluid Dynamics, Bricktown, New Jersey, 1965.